Available online at www.CivileJournal.org

Civil Engineering Journal

(E-ISSN: 2476-3055; ISSN: 2676-6957)

Vol. 10, No. 12, December, 2024

An Advanced Adaptive Mesh for Beam-Column Finite Elements on Transient Dynamic Analysis

Edgar David Mora Martinez [1, 2*], Naser Khaji [1*]

[1] Civil and Environmental Engineering Program, Graduate School of Advanced Science and Engineering, Hiroshima University, Hiroshima 739-8527, Japan.

[2] Departamento de Ingeniería Civil y Ambiental, Escuela Politécnica Nacional (EPN), Quito 170143, Ecuador.

Received 08 August 2024; Revised 19 November 2024; Accepted 27 November 2024; Published 01 December 2024

Abstract

This research examines the influence of truncation error reduction on the nonlinear dynamic analysis of complex framed structures. A modified p-adaptive method, incorporating inertial and damping forces in addition to the common restitutive forces, is introduced to refine the mesh and enhance accuracy. To address convergence challenges arising from increased complexity, Ritz modal shapes are utilized to reconstruct the mass matrix, excluding detrimental modes. The proposed formulation is validated through rigorous computational models and experimental data. Six building case studies, varying in complexity, were analyzed using the modified p-adaptive method. The results revealed substantial variations in frequency and displacement responses, ranging from 6% to 50% and 0.8% to 63%, respectively. These disparities underscore the significant influence of nonlinear behavior on structures with high-order shape functions. The proposed formulation is theoretically more accurate. Therefore, the findings emphasize the necessity of employing mesh refinement techniques to obtain accurate nonlinear dynamic analysis results, particularly for complex structures with pronounced nonlinear characteristics. This study contains the background of a software called MainModelingStr.

Keywords: Beam-Column Elements; High-Order Elements; Nonlinear Elements; p - adaptivity; Generalized Alpha Method; Dynamic Analysis.

1. Introduction

The potential for significant earthquake damage to buildings and infrastructure necessitates rigorous analysis of complex structures. While studies on smaller experiments (plates subjected to static loads) have explored the benefits of mesh refinement for reducing truncation error in simulations [1-4], the impact of this technique on complex buildings under dynamic loads remains largely unexplored. The complexity of modeling such structures, coupled with increased numerical instability and computational demands, has hindered in-depth investigations [5, 6]. This study aims to address this gap by presenting a suitable mesh refinement method for the dynamic analysis of buildings and overcoming the associated challenges.

The primary objective is to minimize truncation error by refining the mesh. This error arises from inconsistencies between equilibrium-compatibility analysis and interpolation functions. Increasing the number of elements or the order of interpolation functions can address this issue. However, modifying all elements introduces challenges such as increased structural complexity, round-off error, and analysis time. To mitigate these effects, this study focuses on increasing the order of interpolation functions rather than the number of elements. This approach is more effective in reducing truncation errors while maintaining a manageable level of complexity [7].

* Corresponding author: edgar.mora@epn.edu.ec; nkhaji@hiroshima-u.ac.jp

http://dx.doi.org/10.28991/CEJ-2024-010-12-01

While a few studies have demonstrated the effectiveness of high-order beam-column elements, their application to nonlinear transient dynamic analysis remains limited. For example, Eisenträger et al. [3] investigated the impact of increasing polynomial order for element compatibility and shape functions in elastic systems under static forces. Bai et al. [8] developed a nonlinear beam-column element with 16 degrees of freedom. Sharifnia [9] proposed a theory for high-order elements to address large deformations, addressing a gap in the literature. This study aims to contribute to this area by exploring the use of high-order beam-column elements for nonlinear transient dynamic analysis.

This study employs a finite element formulation that increases shape function order, leading to a corresponding increase in degrees of freedom and structural complexity. To minimize complexity, the shape function order is modified only for the most influential elements [10]. A p-adaptive method [11] is adapted for beam-column elements, building upon previous applications to static loads or response spectrum methods [12]. To address dynamic analyses, the error formulation for this p-adaptive method incorporates inertial and damping internal forces, which is different from other studies. A significant challenge in this investigation was managing divergence problems in complex structures with high-order elements while maintaining a competitive computational time.

The present study uses implicit algorithms for time-history analyses. In general, implicit algorithms for time-history analyses are faster for large buildings than explicit algorithms since the last ones need to reduce the ground motion time steps, increasing the analysis runtime. Moreover, explicit analyses might introduce a significant period error due to a period elongation [13]. However, implicit integration algorithms sometimes have convergence problems [14, 15], which is the following point to be addressed in this study.

Analyzing complex structures may lead to unexpected phenomena, particularly numerical instability [16, 17]. While some researchers have interpreted numerical instability as a potential indicator of building collapse [18-20], it is actually attributed to the numerical integration algorithm [21-24]. Numerous studies have focused on mitigating convergence and numerical instability issues in dynamic analysis. For instance, Abuteir et al. [25] employed a reduced integration scheme to address instability in functionally graded material plates, utilizing soft higher-order deformation modes. They implemented an implicit time integration method combining the trapezoidal rule and Euler backward methods to handle nonlinearities. However, this method can fall into the hourglass mode phenomenon. Other researchers, such as Song et al. [26] and Ji & Xing [27], have developed time integration schemes based on a state space formulation. However, state space-based approaches can lead to the state space explosion problem in complex structures, potentially resulting in inaccurate results. The state space explosion occurs when the number of possible states in a system grows exponentially, exceeding computational memory limits [28]. While high-order accuracy methods offer advantages [29], they often require more computational time than second-order methods, particularly for complex structures [26]. Generalized alpha approaches, on the other hand, provide faster performance and can reduce spurious frequencies that may cause system divergence. Nevertheless, they may not guarantee energy-momentum conservation, potentially leading to instability [30]. Considering these factors, the present study adopts a generalized alpha method due to its speed and efficiency. Since numerical instabilities can still occur, as shown in the following sections, additional spurious vibrations will be eliminated by limiting no necessary modal shapes reconstructing the mass matrix using Ritz modes.

In summary, this research aims to reduce intrinsic errors in dynamic nonlinear analyses while maintaining efficiency. A p-adaptive method is employed to decrease truncation error by increasing element shape function orders. Unlike previous applications primarily focused on static loads [31], this study introduces a p-adaptive method formulation for dynamic analyses. However, p-adaptive methods can increase structural complexity and round-off error in large structures, leading to convergence issues [32]. To address this problem, the convergence process is enhanced by considering only modal shapes that significantly influence building movement in specific directions. This approach is implemented indirectly, without affecting computational time, thereby improving the performance of the generalized alpha method. To validate the developed software, it was initially tested against a simplified single-degree-of-freedom model and compared with existing software, Seismostruct and OpenSees. Additionally, the results of typical structural analyses of complex buildings were verified against OpenSees, a widely recognized and validated software. Due to the scarcity of detailed data on models and results from other studies for complex structures under transient dynamic loads, the analysis was also compared against a smaller-scale experiment.

The key contributions of this study are (1) a novel p-adaptive method formulation for dynamic analyses, (2) a strategy to improve the convergence of the Newton-Raphson method by excluding irrelevant modal shapes from the mass matrix, and (3) a demonstration of the significance of the p-adaptive method through analyses of various structural complexities and conditions.

The remainder of this paper is organized as follows: Section 2 defines the mathematical background, starting with error calculations and the proposed p-adaptive method. Afterward, a strategy for nonlinear models is given. Additionally, convergence problems are discussed, and a solution is proposed. Section 3 validates the proposed formulation and strategy through two computational and one actual experiment. Section 4 describes the numerical examples used herein. Section 5 shows the results and discusses using the proposed p-adaptive method. Finally, the paper is concluded in Section 6.

2. Mathematical Backgrounds

The truncation error is quantified by analyzing the internal work in each element according to the interpolation functions and the theoretical forces from the constitutive laws, inertia, and damping. Additionally, the truncation and round-off error are compared since both were normalized to be one for the optimal error, which is the maximum allowed error. Thus, when the truncation error equals one, the error is equal to an error uniformly distributed in all the elements [11]. Hence, if no element errors are greater than one, no elements govern this error. Furthermore, the round-off error of one is the maximum allowed error regarding the loss of significant digits [33]. A flowchart is exposed at the end of this section.

2.1. Basic Definitions

The truncation error in structural analysis occurs because the polynomial used to represent each element displacement is based on a third-order polynomial and the rotations on a second-order polynomial, as follows:

$$\bar{v}_z(x) = \alpha_0 x^0 + \alpha_1 x^1 + \alpha_2 x^2 + \alpha_3 x^3 \quad (1)$$

$$\bar{\theta}_y(x) = \bar{v}'_Z(x) = \alpha_1 x^0 + 2\alpha_2 x^1 + 3\alpha_3 x^2 \quad (2)$$

where x is the distance to any point of the element, $\bar{v}_z(x)$ indicates the continuous transverse displacement, $\bar{\theta}_y(x)$ is the rotation angle, and α_i's are polynomial constants. However, the order of those polynomials can be increased, reducing the truncation error. The equations in this study have been only developed for the local plane xz from Figure 1, and they can be transformed for the plane xy. The axial and torsional forces are omitted for the demonstration, but they can be calculated analogously with the Lagrangian interpolation, which is a more straightforward case. Moreover, in this study, the rotation order equation is used to denominate the order of bending elements; thus, the traditional elements ((1) and (2)) are called second-order elements.

The truncation error can be reduced by locating the elements with the most influential internal forces and increasing their shape function order (p-adaptive). Since the ground motions can change their main frequencies in different intervals, the elements whose order will increase and decrease might change. Then, in the present study, the p-adaptive method will be run in every $\underline{n}$ steps of the time-history analysis before some elements yield. After the elements have reached the nonlinear range, the order of the shape functions should also change, but this could increase convergence problems because of sharp changes in the stiffness. Therefore, the p-adaptive method evaluation is recommended to stop when a nonlinear behavior has started.

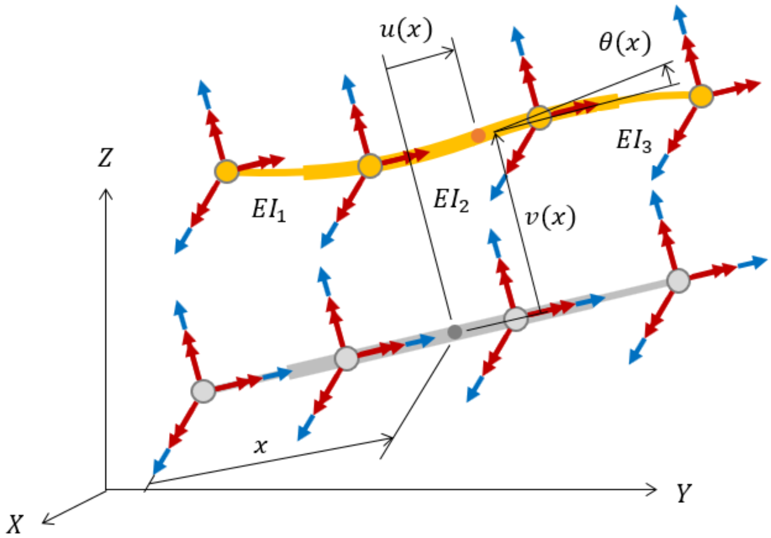

Figure 1. A typical high-order beam-column finite element

The shape function order refinement for the p-adaptive frame structure method is first stated as follows. To this end, Equations 1 and 2 are generalized by:

$$\bar{v}_z(x) \cong \sum_{j=0}^{n'+1} \alpha_j x^j \quad (3)$$

$$\bar{\theta}_y(x) = \bar{v}'_Z(x) \quad (4)$$

thereby:

$$\bar{v}_z(x) = \underline{\boldsymbol{N}}\, {}^{el}\boldsymbol{d} \tag{5}$$

where $\underline{\boldsymbol{N}}$ is a horizontal vector containing the shape functions related to the displacements DOF, $\boldsymbol{d}$, and el is a structural element ($el \in \boldsymbol{\Omega}$) where $\boldsymbol{\Omega}$ denotes the entire domain of the structure. For the demonstration ${}^{el}\boldsymbol{d} = {}^{el}\boldsymbol{d}^{xz}$, and it is sorted as follows in this study:

$$^{el}\boldsymbol{d} = \left\{v_{z_0}, \theta_{y_1}, v_{z_2}, \theta_{y_3}, \dots, v_{z_j}, \theta_{y_{j+1}}, \dots, v_{z_{n'}}, \theta_{y_{n'+1}}\right\}^{\mathrm{T}} \tag{6}$$

where each element node contains a displacement DOF, v_{z_j}, and a rotational DOF, $\theta_{y_{j+1}}$. Also, n' is the order of the polynomial $\bar{\theta}_y(x)$.

When increasing the order in an element, the new system will have to deal with more DOFs. Regarding the Runge phenomenon, a different distribution of nodes from equidistant locations, like Lobatto, Legendre, or Chebyshev approaches, should be used for the high-order elements. Previous works have shown remarkable results with the Lobatto and Chebyshev node distributions for high-order interpolations [34].

In finite element methods, the base stiffness matrix of one element is defined as:

$$^{el}\boldsymbol{K} = \int_0^L \boldsymbol{B}^{\mathrm{T}}\boldsymbol{D}\boldsymbol{B}\,\partial x \tag{7}$$

where $\boldsymbol{B}$ is:

$$\boldsymbol{B} = \mathcal{L}_2\underline{\boldsymbol{N}}, \tag{8}$$

in which $\mathcal{L}_2$ represent a second-order derivative, and $\boldsymbol{D}$ indicates the element's material properties. It is essential to mention that the Hermite interpolation is used for the shape functions $\underline{\boldsymbol{N}}$, as shown in different references [35-38].

2.2. Truncation Error

Considering the Hamilton principle, we have the internal forces in each element ${}^{el}\bar{f}$ as:

$$^{el}\bar{f} = {}^{el}\bar{f}_d + {}^{el}\bar{f}_v + {}^{el}\bar{f}_a \tag{9}$$

where ${}^{el}\bar{f}_d$, ${}^{el}\bar{f}_v$, and ${}^{el}\bar{f}_a$ are the restoring, dissipative, and inertial forces, respectively. ${}^{el}\bar{f}_d$ is the force in each element calculated with constitutive and kinematics considerations [39] expressed by:

$$^{el}\bar{f}_d = D\mathcal{L}_b\underline{\boldsymbol{N}}\, {}^{el}\boldsymbol{d} \tag{10}$$

where $D = EI$ indicates the element's flexural rigidity (see Figure 1), and $D\mathcal{L}_b\underline{\boldsymbol{N}}$ is the constitutive law. $\mathcal{L}_b$ is a formal operator that represents a b-order derivative. For bending forces, $b = 2$ so that $\mathcal{L}_b\underline{\boldsymbol{N}}\, {}^{el}\boldsymbol{d}$ is the curvature. In the case of working with axial forces and torsional forces, $b = 1$ so that $\mathcal{L}_b\underline{\boldsymbol{N}}\, {}^{el}\boldsymbol{d}$ is the axial strain and the torsional shear strain, respectively.

The inertial force ${}^{el}\bar{f}_a$ can be taken as [13]:

$$^{el}\bar{f}_a = \gamma\underline{\boldsymbol{N}}\, {}^{el}\ddot{\boldsymbol{d}} \tag{11}$$

where γ is the mass per unit length, and ${}^{el}\ddot{\boldsymbol{d}}$ is the acceleration in each DOF of the element el.

In the case of a dissipative force, the classic damping matrix is obtained to achieve its orthogonality with the modal matrix calculated with the mass and stiffness matrix. Thus, the damping matrix of each element ${}^{el}\boldsymbol{C}$ can be calculated in the same way and then ${}^{el}\bar{f}_v$ be deduced. The Rayleigh method is used in this research. Therefore, this force must be a function of the constitutive law of the forces ${}^{el}\bar{f}_a$ and ${}^{el}\bar{f}_d$ to obtain consistent results since these constitutive laws are used to calculate the mass and stiffness matrices. Hence, ${}^{el}\bar{f}_v$ can be calculated as:

$$^{el}\bar{f}_v = (\alpha_0\gamma + \alpha_1\boldsymbol{D}\mathcal{L}_b)\underline{\boldsymbol{N}}\, {}^{el}\dot{\boldsymbol{d}} \tag{12}$$

where α_0 and α_1 are the Rayleigh coefficients calculated with the first mode frequencies [13], and ${}^{el}\dot{\boldsymbol{d}}$ is the velocity in each DOF of the element el.

Structural analysis is enhanced by finding the elements that influence the behavior the most. Finding the mentioned elements is the goal of the p-adaptive method. In the p-adaptive method, the loads are usually used, but work will be used subsequently to consider different types of forces, e.g., axial forces, bending forces, etc. Thus, the first goal is to reduce the following error of each element:

$$\acute{e} = {}^{el}\bar{f}^{*} - {}^{el}\bar{f} \tag{13}$$

The remaining unknown term, ${}^{el}\bar{f}^{*}$, is the force at any point x, interpolated with the shape functions from the prescribed forces $\boldsymbol{f}^{*}$ in the element's DOF as described below:

$${}^{el}\bar{f}^{*} = \underline{\boldsymbol{N}}^{el}\boldsymbol{f}^{*} \tag{14}$$

The assumption taken in Equation 14 is made since it is considered that every element segment satisfies a linear correspondence between displacement and forces, even in nonlinear analyses, for every iteration uses a corresponding linear force-displacement relation.

The work from the prescribed force $\boldsymbol{f}^{*}$ can be obtained by substituting Equations 10 and 14 to into Equation 13 and knowing that the error $\acute{e}$ should be zero. This equation results in:

$$\underline{\boldsymbol{N}}^{el}\boldsymbol{f}^{*} - \left(\boldsymbol{D}\mathcal{L}_b\underline{\boldsymbol{N}}\,{}^{el}\boldsymbol{d} + \gamma\underline{\boldsymbol{N}}\,{}^{el}\ddot{\boldsymbol{d}} + \alpha_1\boldsymbol{D}\mathcal{L}_b\underline{\boldsymbol{N}}\,{}^{el}\dot{\boldsymbol{d}} + \alpha_0\gamma\underline{\boldsymbol{N}}\,{}^{el}\dot{\boldsymbol{d}}\right) = 0 \tag{15}$$

It is possible to isolate the force $\boldsymbol{f}^{*}$after multiplying each term by $\underline{\boldsymbol{N}}^{\mathrm{T}}$ and integrating the equation, this is expressed as follows:

$$\int_0^L \left(\underline{\boldsymbol{N}}^{\mathrm{T}}\underline{\boldsymbol{N}}^{el}\boldsymbol{f}^{*} - \underline{\boldsymbol{N}}^{\mathrm{T}}\left(\boldsymbol{D}\mathcal{L}_b\underline{\boldsymbol{N}}\,{}^{el}\boldsymbol{d} + \gamma\underline{\boldsymbol{N}}\,{}^{el}\ddot{\boldsymbol{d}} + \alpha_1\boldsymbol{D}\mathcal{L}_b\underline{\boldsymbol{N}}\,{}^{el}\dot{\boldsymbol{d}} + \alpha_0\gamma\underline{\boldsymbol{N}}\,{}^{el}\dot{\boldsymbol{d}}\right)\right)\partial x = 0 \tag{16}$$

which results in:

$${}^{el}\boldsymbol{f}^{*} = \left(\int_0^L \underline{\boldsymbol{N}}^{\mathrm{T}}\underline{\boldsymbol{N}}\partial x\right)^{-1}\left(\int_0^L \boldsymbol{D}\mathcal{L}_{\mathrm{b}}\underline{\boldsymbol{N}}\,{}^{el}\boldsymbol{d}\,\partial x + \int_0^L \gamma\underline{\boldsymbol{N}}\,{}^{el}\ddot{\boldsymbol{d}}\,\partial x + \alpha_1\int_0^L \boldsymbol{D}\mathcal{L}_{\mathrm{b}}\underline{\boldsymbol{N}}\,{}^{el}\dot{\boldsymbol{d}}\,\partial x + \alpha_0\int_0^L \gamma\underline{\boldsymbol{N}}\,{}^{el}\dot{\boldsymbol{d}}\,\partial x\right) \tag{17}$$

The error in each DOF of each element can be calculated using a residual work to involve distinct types of forces by:

$${}^{el}\boldsymbol{e} = \frac{1}{2}\,{}^{el}\boldsymbol{d} \odot \left(\int_0^L \underline{\boldsymbol{N}}^{el}\boldsymbol{f}^{*}\partial x - \int_0^L {}^{el}\bar{f}\,\partial x\right) \tag{18}$$

where $\odot$ represents the Hadamard product. The entire system error can be obtained by the following norm:

$$\|\boldsymbol{e}\| = \left[\sum_{el=1}^{nel}({}^{el}\boldsymbol{e})^{\mathrm{T}}({}^{el}\boldsymbol{e})\right]^{\frac{1}{2}} \tag{19}$$

The error will be normalized, assuming that the error is uniformly distributed in the entire system [11], which leads to:

$$\bar{e}_{nel} = \bar{\eta}\left[\frac{\left\|\frac{1}{2}{}^{el}\boldsymbol{d}\odot\boldsymbol{f}\right\|^2}{nel}\right]^{\frac{1}{2}} \tag{20}$$

This permissible error depends on the number of elements of the entire system nel, and the maximum permissible error $\bar{\eta}$. In linear analyses, $\bar{\eta}$ will be established after various iterations. Nonetheless, in time-history analyses, $\bar{\eta}$ is obtained within the steps of the procedures, where the global results will not be affected. $\bar{\eta}$ is obtained by the maximum error of each element's DOF (el_{DOF}) of all the elements:

$$\bar{\eta} \approx \max_{el\in\{1,\ldots,\Omega\}}\left(\max_{DOF\in\{1,\ldots,n'+1\}}\left(\frac{{}^{el_{\mathrm{DOF}}}e}{\frac{1}{2}{}^{el_{\mathrm{DOF}}}\boldsymbol{d}\odot{}^{el_{\mathrm{DOF}}}\boldsymbol{f}}\right)\right) \tag{21}$$

Finally, the error normalized for each element is given as:

$${}^{el}\xi = \frac{\|{}^{el}\boldsymbol{e}\|}{\bar{e}_{nel}} \tag{22}$$

from which the order n' must be refined when ${}^{el}\xi$>1. The order will increase by one each time refinement is required.

2.3. Round-off Error

It is known that when the truncation error has decreased, the round-off error will increase, which will be important for adaptive methods in the finite element formulation [40]. The round-off error is caused by a loss of significant digits, n_{lost}. Although this last error depends on the machine and other hardware details, it can be roughly calculated with the condition number operator $\bar{\kappa}(\blacksquare)$ of $\boldsymbol{M}^{-1}\boldsymbol{S}$ (the inverse of the structural mass matrix multiplied by the structural stiffness matrix) as given by Cheney & Kingaid [41]:

$$\bar{\kappa}(\boldsymbol{M}^{-1}\boldsymbol{S}) = \|\boldsymbol{M}^{-1}\boldsymbol{S}\|_2 \|(\boldsymbol{M}^{-1}\boldsymbol{S})^{-1}\|_2 = \frac{\bar{\sigma}_{\max}(\boldsymbol{M}^{-1}\boldsymbol{S})}{\bar{\sigma}_{\min}(\boldsymbol{M}^{-1}\boldsymbol{S})} \tag{23}$$

in which $\|\blacksquare\|_2$ denotes the Euler norm, and

$$\bar{\sigma}_{\min}(\boldsymbol{M}^{-1}\boldsymbol{S}) = \min\sqrt{|\lambda((\boldsymbol{M}^{-1}\boldsymbol{S})^{\mathrm{T}}\boldsymbol{M}^{-1}\boldsymbol{S})|} \tag{24-a}$$

$$\bar{\sigma}_{\max}(\breve{\boldsymbol{A}}) = \max\sqrt{|\boldsymbol{\lambda}((\boldsymbol{M}^{-1}\boldsymbol{S})^{\mathrm{T}}\boldsymbol{M}^{-1}\boldsymbol{S})|} \tag{24-b}$$

where $\boldsymbol{\lambda}(\blacksquare)$ is the eigenvalues vector. Hence, the condition number turns out to be:

$$\bar{\kappa}(\boldsymbol{M}^{-1}\boldsymbol{S}) = \frac{\omega_{\max}^2}{\omega_{\min}^2} \tag{25}$$

where $\omega_{\max}$ and $\omega_{\min}$ are the maximum and minimum natural frequencies of the analyzed structure.

The limit of the condition number can be imposed with the machine epsilon number ε, which is equivalent to the decimal significant digits available to work [33]. The upper limit used is $1/\sqrt{\varepsilon}$ [42], and therefore, the normalized error by one is given as:

$$\xi_{\text{round-off}} = \frac{\omega_{\max}^2}{\omega_{\min}^2}\sqrt{\varepsilon} \tag{26}$$

This proposal calculates the round-off error after each refinement iteration from the truncation-error control to stop the refinement process.

2.4. Variation of the Cross-Section Stiffness

The study of nonlinear behavior in buildings is a paramount concern in structural analysis, particularly within the context of seismic events. Nonlinearities are often concentrated in specific regions of the structure, known as plastic hinges. Consequently, a comprehensive understanding of plastic hinges is imperative. The distributed plasticity hinge approach, which accounts for continuous displacements, is widely recognized as a more realistic representation of nonlinear behavior compared to traditional idealizations [43]. While the flexibility method (or force method) can be employed to analyze distributed plasticity hinges using in-series spring idealizations [44, 45], its applicability is limited to systems of lower order. The primary challenge arises from the necessity of introducing additional degrees of freedom (DOFs) to the corotational coordinate system, which is incompatible with the flexibility method due to the singularity of their flexibility matrix, hindering inversion and subsequent derivation of the stiffness matrix.

The strain energy has been considered to calculate the moments (and other forces) for the rigidity evaluation in each time-history analysis instant i as follows:

$${}^{el}\hat{u}_i = \sum_{r=1}^{\bar{n}}\left({}^{el}\hat{u}_{\mathrm{r_i}}\right) \tag{27}$$

in which ${}^{el}\hat{u}_{\mathrm{r}}$ contains the contribution for the energy of each section with a different nonlinear plastic length rigidity r from 1 to $\bar{n}$, as indicated in Figure 2. This last equation leads to:

$${}^{el}\hat{u}_{\mathrm{r_i}} = \frac{1}{2}\,{}^{el}\boldsymbol{\theta}_i^{\mathrm{T}}\,{}^{el}\boldsymbol{m}_{r_i} \tag{28}$$

where ${}^{el}\boldsymbol{m}_{r_i}$ are the partial moments that correspond to the nonlinear plastic length rigidity, and ${}^{el}\boldsymbol{\theta}_i$ is a vector that contains the rotation of each DOF related to ${}^{el}\boldsymbol{m}_{r_i}$.

Equation 28 can be used, provided that the element's partial stiffness ${}^{el}\boldsymbol{K}_{r_i}$, which is dependent on ${}^{el}\overline{EI}_r(x)$, uses continuous functions for the rigidity ${}^{el}\overline{EI}_r(x)$ along the element length. Thus, sets of continuous sigmoid functions can be used to represent continuous rigidity as follows:

$$ {}^{el}\overline{EI}_r(x) = EI_r\left(\sigma\left(x - \sum_{g=1}^{r-1} l_g\right) - \sigma\left(x - \sum_{g=1}^{r} l_g\right)\right) \tag{29}$$

where $\sigma(\blacksquare)$ is a Sigmoid function expressed by

$$\sigma(\blacksquare) = \frac{1}{1+\exp(-\max({}^{el}\boldsymbol{EI}_r)\blacksquare)} \tag{30}$$

in which ${}^{el}\boldsymbol{EI}_r$ contains all the flexural rigidities in one element (see Figure 2).

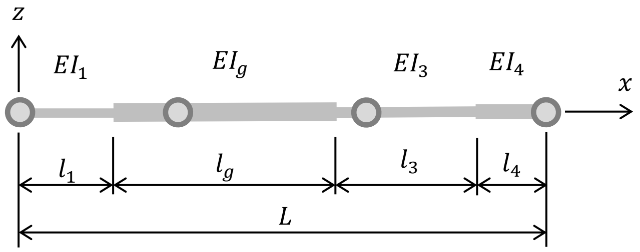

Figure 2. A typical high-order beam-column finite element

The partial moment ${}^{el}\boldsymbol{m}_{r_i}$ can be calculated in every step i using the curvature ${}^{el}\boldsymbol{\varphi}$ as the following relation:

$${}^{el}\boldsymbol{m}_{r_i} = {}^{el}\boldsymbol{m}_{r_{i-1}} + {}^{el}\boldsymbol{EI}^{\mathrm{T}}_{r\,i-1}({}^{el}\boldsymbol{\varphi}_i - {}^{el}\boldsymbol{\varphi}_{i-1}) \tag{31}$$

where the curvature is calculated using the shape functions related to the rotation DOFs, $\underline{\boldsymbol{N}}_\theta$, as:

$${}^{el}\boldsymbol{\varphi} = \left(\int_0^L \underline{\boldsymbol{N}}_\theta{}^{\mathrm{T}} \underline{\boldsymbol{N}}_\theta \partial x\right) {}^{el}\boldsymbol{\theta} \tag{32}$$

and ${}^{el}\boldsymbol{EI}^{\mathrm{T}}_{r\,i}$ is the rigidity components in every section r, written as:

$${}^{el}\boldsymbol{EI}^{\mathrm{T}}_{r\,i} = \left\{{}^{el}EI_g \middle| g \in \{\text{evaluated sections}\}\right\}^{\mathrm{T}} \tag{33}$$

The evaluated rigidity EI_g in the instant i is found by evaluating the rules of the moment-curvature model, the fiber method, or any other. This procedure has also been used analogously for axial and torsional forces in the preformed examples. In the end, these rigidities are used to calculate the stiffness matrix of each corotated element, which can be limited to only the section of the element's ends.

2.5. Moment Curvature Model

The fiber method with the Ramberg-Osgood model has been utilized to represent the behavior of each cross-section fiber. This method consists of dividing each cross-section into small segments called fibers. The fibers represent the confined concrete, unconfined concrete, and steel rebars for each reinforced concrete element. The increment of the curvatures in each step ${}^{el}\Delta\boldsymbol{\varphi}_i$ is used to calculate the strain ${}_{fiber_j}^{el}\Delta\boldsymbol{\varepsilon}_i$ of each fiber j assuming that flat sections remain flat after deformation [46] in the following way:

$${}_{fiber_j}^{el}\Delta\boldsymbol{\varepsilon}_i = {}_{fiber_j}^{el}\boldsymbol{h}_{PNA}\; {}^{el}\Delta\boldsymbol{\varphi}_i + \frac{{}^{el}\Delta\boldsymbol{d}_{axial_i}}{{}^{el}L} \tag{34}$$

where ${}^{el}\Delta\boldsymbol{\varphi}_i$ is the resultant of the increment of curvatures in the basic system axis x and y of the element el, ${}_{fiber_j}^{el}\boldsymbol{h}_{PNA}$ indicates a vector containing the perpendicular distance from the plastic neutral axis (PNA) to each fiber, ${}^{el}\Delta\boldsymbol{d}_{axial_i}$ is a vector with the axial displacement from the time history analysis of each element, and ${}^{el}L$ denotes the length of each element. The PNA is found by numerical methods.

The jth fiber, $fiber_j$, is analyzed to obtain its modulus of elasticity ${}_{fiber_j}^{el}\boldsymbol{E}$. The modulus is the same as the elastic modulus ${}_{fiber_j}^{el}\boldsymbol{E}_0$ if the fiber stress is in the unloading phase. Otherwise, the Ramberg-Osgood model is used. Afterward, the stress of each fiber is calculated as follows:

$${}_{fiber_j}^{el}\boldsymbol{\sigma}_i = {}_{fiber_j}^{el}\boldsymbol{E}\, {}_{fiber_j}^{el}\Delta\boldsymbol{\varepsilon}_i + {}_{fiber_j}^{el}\boldsymbol{\sigma}_{i-1} \tag{35}$$

The Ramberg-Osgood equation is used to obtain the stress of every fiber in the loading phase since this equation represents the hysteresis behavior of each element. Numerical methods are employed to obtain the stress from the following equation:

$$ {}^{el}_{fiber_j}\varepsilon_i = \frac{{}^{el}_{fiber_j}\sigma_i}{{}^{el}_{fiber_j}E_0}\left(1 + \bar{\alpha}\,\mathrm{abs}\left(\frac{{}^{el}_{fiber_j}\sigma_i}{{}^{el}_{fiber_j}\sigma_y}\right)^{\bar{n}-1}\right) + {}^{el}_{fiber_j}\varepsilon_{fix_i} \tag{36} $$

where ${}^{el}_{fiber_j}\sigma_y$ is the yield stress of the fiber j, ${}^{el}_{fiber_j}\varepsilon_{fix_i}$ is the strain saved in each step of the unloading phase, and $\bar{\alpha}$ and $\bar{n}$ are equation coefficients, where $\bar{\alpha}$ is $200\mathrm{abs}\left({}^{el}_{fiber_j}\sigma_y / {}^{el}_{fiber_j}E_0\right)$ and $\bar{n} = 6$, which are values usually used [47]. Also, $\mathrm{abs}(\blacksquare)$ denotes the absolute value of $\blacksquare$.

2.6. Structural Analysis Procedure

An implicit time-history analysis is more convenient for reducing the algorithm's running time. As stated before, some of the faster and more robust procedures are the generalized alpha methods (GAM). Those belong to the direct integration implicit procedures derived from the Newmark type analysis. Since the GAM can reduce spurious vibration, this analysis is ideal for high-order elements.

The well-known Newmark method uses the coefficients β and γ, and the displacements $\boldsymbol{q}_i$, velocities $\dot{\boldsymbol{q}}_i$, and accelerations $\ddot{\boldsymbol{q}}_i$ for each global system DOF in every instant i. The GAM enhances the convergence of the movement equation determined by:

$$ \boldsymbol{M}\ddot{\boldsymbol{q}}_{i+1} + \boldsymbol{C}_{i+1}\dot{\boldsymbol{q}}_{i+1} + \boldsymbol{S}_{i+1}\boldsymbol{q}_{i+1} = \boldsymbol{r}_{i+1} \tag{37} $$

where $\boldsymbol{M}$, $\boldsymbol{C}$, and $\boldsymbol{S}$ are the global mass, damping, and stiffness matrices of the structure, respectively. Moreover, $\bar{\boldsymbol{r}}$ is the external forces vector. The convergence will be found in the time $t_{i+1-\alpha_f}$, which is $t_{n+1} - \alpha_f(t_{n+1} - t_n)$. Additionally, the acceleration will vary α_m times. Hence, we can express this idea as follows:

$$ (\boldsymbol{M}\ddot{\boldsymbol{q}}_{i+1} + \boldsymbol{C}_{i+1}\dot{\boldsymbol{q}}_{i+1} + \boldsymbol{S}_{i+1}\boldsymbol{q}_{i+1}) - \left(\boldsymbol{M}(\ddot{\boldsymbol{q}}_{i+1} - \ddot{\boldsymbol{q}}_i)\alpha_m + \boldsymbol{C}_{i+1}(\dot{\boldsymbol{q}}_{i+1} - \dot{\boldsymbol{q}}_i)\alpha_f + \boldsymbol{S}_{i+1}(\boldsymbol{q}_{i+1} - \boldsymbol{q}_i)\alpha_f\right) = \boldsymbol{r}_{i+1} - (\boldsymbol{r}_{i+1} - \boldsymbol{r}_i)\alpha_f \tag{38} $$

Thus, isolating terms, the following equation can then be found and solved using the Newmark process:

$$ \boldsymbol{M}\ddot{\boldsymbol{q}}_{i+1-\alpha_m} + \boldsymbol{C}_{i+1}\dot{\boldsymbol{q}}_{i+1-\alpha_f} + \boldsymbol{S}_{i+1}\boldsymbol{q}_{i+1-\alpha_f} = \boldsymbol{r}_{i+1} \tag{39} $$

where

$$ \boldsymbol{q}_{i+1-\alpha_f} = (1 - \alpha_f)\boldsymbol{q}_{i+1} + \alpha_f\boldsymbol{q}_i \tag{40} $$

$$ \dot{\boldsymbol{q}}_{i+1-\alpha_f} = (1 - \alpha_f)\dot{\boldsymbol{q}}_{i+1} + \alpha_f\dot{\boldsymbol{q}}_i \tag{41} $$

$$ \ddot{\boldsymbol{q}}_{i+1-\alpha_m} = (1 - \alpha_m)\ddot{\boldsymbol{q}}_{i+1} + \alpha_m\ddot{\boldsymbol{q}}_i \tag{42} $$

$$ \boldsymbol{r}_{i+1-\alpha_f} = (1 - \alpha_f)\boldsymbol{r}_{i+1} + \alpha_f\boldsymbol{r}_i \tag{43} $$

Many researchers have studied the relationship between the coefficients β, γ, α_f, and α_m in the pro of preventing divergence problems in structural analyses [30]. The parameters that adjust better to the problem here studied, i.e., structures, are proposed by Chung-Hulbert as follows:

$$ \beta = \frac{1}{4}(1 - \alpha_m + \alpha_f)^2 \tag{44} $$

$$ \gamma = \frac{1}{2} - \alpha_m + \alpha_f \tag{45} $$

The alpha coefficients are related to ρ_∞ as indicated below:

$$ \alpha_m = \frac{2\rho_\infty - 1}{\rho_\infty + 1} \tag{46} $$

$$ \alpha_f = \frac{\rho_\infty}{\rho_\infty + 1} \tag{47} $$

in which the value of ρ_∞ will be between 0 and 1. It is worth noting that the smaller ρ_∞ is, the larger the velocity overshooting will be, which is a harmful effect [30].

Additionally, structural analyses using the Ritz modes might be used to avoid spurious vibration in a physically improbable direction [48, 49]. However, the analysis of Ritz modes changing every instant can be computationally intensive and must be used with discretion.

2.7. Numerical Method Error from Instability and Spurious Vibration

In transient dynamic analyses of complex structures, the "numerical instability" can be perceived as an uncontrolled oscillation, divergence in iterative solvers, or excessive displacements. This behavior could be given for the integration method, time step size, damping, and model nonlinearities [50, 51]. On the other hand, "spurious vibration" can be seen when unrealistic or unexpected patterns are found in the modal shapes, which could evocate numerical instabilities [52]. Another phenomenon encountered is a "counterintuitive moment-curvature" behavior. It can occur in complex structures when nonlinearities appear, which can cause the moment-curvature response to go in an unexpected direction opposite to an assumed behavior, e.g., the rules of the Takeda concrete model [53]. It is essential to mention that these phenomena can or cannot be related.

A counterintuitive moment-curvature behavior is corrected using a moment-curvature model that smooths the transition between rigidities changes. This is another reason for using the Ramberg-Osgood model above described since it provides a smooth transition.

2.8. Numerical Method Error from Instability And Spurious Vibration

The unexpected phenomena can be significantly reduced by decreasing the coefficient ρ_∞ of the GAM. However, this action can present misleading results because of the increase in velocity overshooting, in addition to large time-step size problems or simply numerical instability for problems with high-order shape functions, particularly if the mesh is not correctly refined. Therefore, because high-order interpolation functions can result in spurious frequencies, Ritz modal shapes using the straightforward Gramm-Schmidt process can prevent excitation in directions that need not be studied [48]. These vibration modes are restricted because, unlike eigenvalue analysis, which produces universal vibrational patterns regardless of external forces, Ritz analysis generates specific mode shapes influenced by the direction of the applied load. This tailored approach ensures that the resulting mode shapes are more closely aligned with the actual behavior of the structure under the given loading conditions. Thus, the mass matrix is filtered from unnecessary modal shapes so that the mass of those unnecessary DOFs can be zero, and thereby, they will not influence the dynamic analyses. Moreover, since the mass matrix will not change each instant, this operation will not affect the running time, as could occur with the stiffness matrix. The modal shapes' filtering is made using the following concept:

$$\widehat{\boldsymbol{M}}\ddot{\boldsymbol{y}} + \widehat{\boldsymbol{C}}\dot{\boldsymbol{y}} + \widehat{\boldsymbol{S}}\boldsymbol{y} = \widehat{\boldsymbol{\Phi}}^{\mathrm{T}}\boldsymbol{r} \tag{48}$$

where $\widehat{\boldsymbol{\Phi}}$ are the Ritz modes normalized using the mass matrix, and $\boldsymbol{y}$, $\dot{\boldsymbol{y}}$, and $\boldsymbol{y}$ are the increment of the structural responses in natural coordinates. The natural coordinates are vectors that scale the Ritz vectors. In addition, the orthogonal mass normalized matrices of (48) are defined as:

$$\widehat{\boldsymbol{M}} = \widehat{\boldsymbol{\Phi}}^{\mathrm{T}}\boldsymbol{M}\widehat{\boldsymbol{\Phi}} \tag{49}$$

$$\widehat{\boldsymbol{C}} = \widehat{\boldsymbol{\Phi}}^{\mathrm{T}}\mathbf{C}\widehat{\boldsymbol{\Phi}} \tag{50}$$

$$\widehat{\boldsymbol{S}} = \widehat{\boldsymbol{\Phi}}^{\mathrm{T}}\boldsymbol{S}\widehat{\boldsymbol{\Phi}} \tag{51}$$

Knowing that $\widehat{\boldsymbol{M}}$ is an identity matrix due to the normalized modes, the following equation can be determined:

$$\widehat{\boldsymbol{\Phi}}^{\mathrm{T}}\boldsymbol{M}\widehat{\boldsymbol{\Phi}} = \boldsymbol{I} \tag{52}$$

The reconstructed $\boldsymbol{M}$ can be obtained by multiplying each term by $\boldsymbol{M}\widehat{\boldsymbol{\Phi}}$ and $\left(\boldsymbol{M}\widehat{\boldsymbol{\Phi}}\right)^{\mathrm{T}}$. Thus, $\boldsymbol{M}$ results in:

$$\boldsymbol{M} = \boldsymbol{M}\widehat{\boldsymbol{\Phi}}\left(\boldsymbol{M}\widehat{\boldsymbol{\Phi}}\right)^{\mathrm{T}} \tag{53}$$

2.9. Procedure Flowchart

The following flowchart displays the procedure used in this work using the previously demonstrated equations (see Figure 3). This procedure is used in a software package made in Python 3 called MainModelingStr. The method starts initializing common parameters for time-history analysis. Afterwards, the mass matrix is reconstructed using the Ritz modes, and the approximated yielding forces ${}^{el}\boldsymbol{f}_d^y$ are calculated using the close-form of Monti and Petrone [54]. In the main loop, each ground motion point is evaluated using the GAM method, and the structure responses are calculated. Next, the nonlinear evaluation of each element will start once any element has overcome the approximated yielding forces. In this case, the approximated yielding forces ${}^{el}\boldsymbol{f}_d^y$ are multiplied by a safety factor to ensure that the nonlinearity of the elements is effectively evaluated. On the other hand, when ${}^{el}\boldsymbol{f}_d^y$ is less than the restitutive forces of each element, the refinement procedure starts.

As indicated before, the refinement process begins by calculating the conditional number, the truncation, and the round-off error. Now, the elements with an error ${}^{el}\xi$ greater than one will be refined. However, the number of refined elements will be limited according to the round-off error. To avoid many computational operations, the maximum number of refined elements ($maximum\ refined\ elements$) is obtained as a simple linear interpolation, as shown in the flowchart. Finally, when elements are refined, the gaps in the structural responses ($\boldsymbol{q}_i$, $\dot{\boldsymbol{q}}_i$, $\ddot{\boldsymbol{q}}_i$) are filled using the interpolation functions $\underline{\boldsymbol{N}}$ on the refined elements (previously presented in Equation 5).

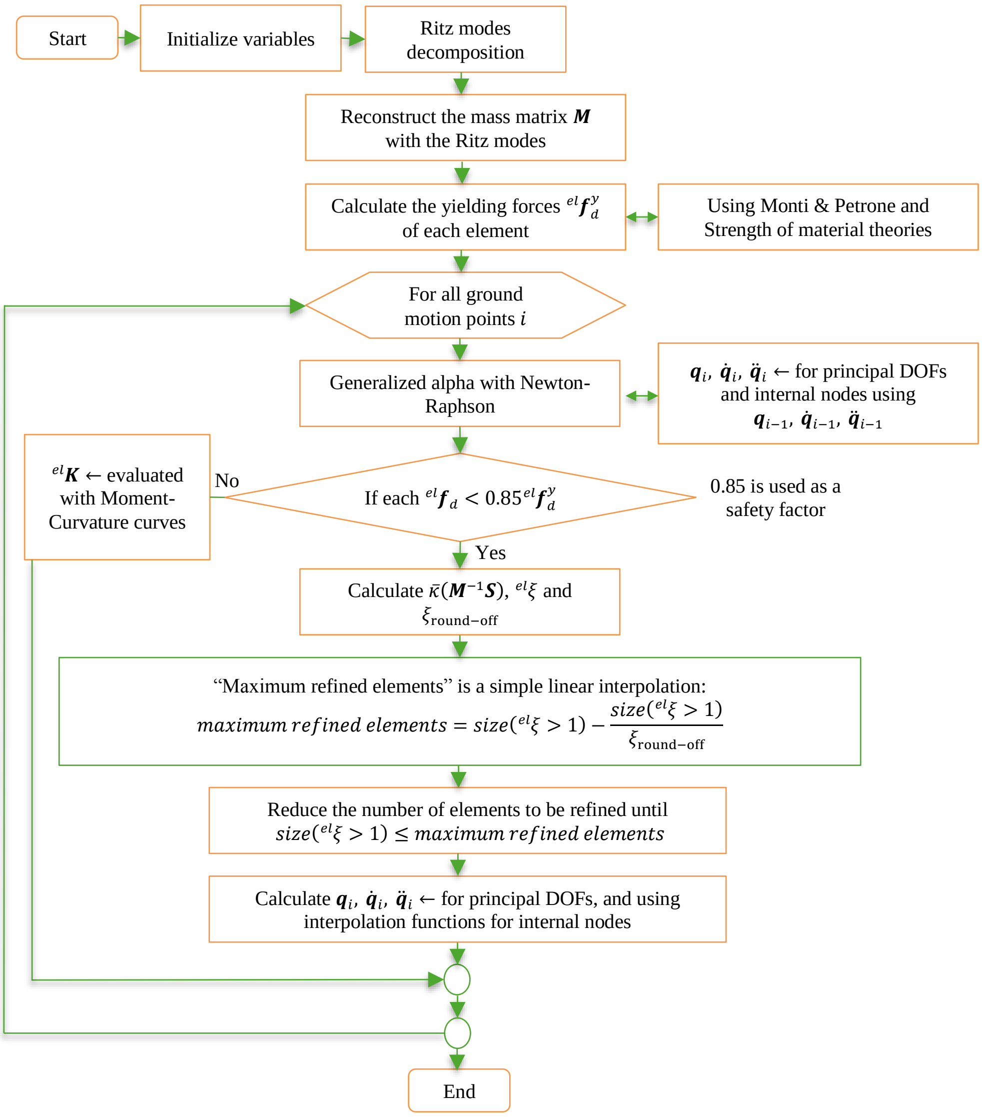

Figure 3. Procedure flowchart for the structural time-history analysis

3. Validation of the Proposed Method

The proposed formulation has been validated as follows. Firstly, it is exhibited that there is an optimal range where the truncation and the round-off error curves cross, which highlights the importance of the p-adaptive method to reduce the total numerical error. Afterward, a case where the proposed strategy is useful is presented. Subsequently, it is shown through a small actual experiment building that the p-adaptive method results are more similar, leaving the window open for future research with more large-scale experiments

3.1. Numerical Method Error from Instability and Spurious Vibration

A small building model is used to validate the truncation and round-off error criteria. The benchmark is the result of this building obtained by solving the differential equation for one degree of freedom. Those results will be compared to the proposed formulation, Seismostruct [55], and OpenSeesPy [56]. The building is a one-floor reinforced concrete structure made of square columns of 0.25×0.25 m^2 with four confined rebars of a diameter of 32 mm. Its beams are rectangular elements of 0.25×0.60 m^2 with six confined rebars of a diameter of 16 mm. A high error was found with these conditions: flexible columns and stiffer beams. The Young modulus of the concrete is 21.5 GPa, the compressive strength is 21 MPa, and the specific weight is 24 kN/m^3. The Young modulus of the rebar is 200 GPa, and the compressive and tensile strength is 590 MPa.

The excitation applied to the structure is a sinusoidal ground acceleration, expressed as follows:

$$\ddot{u}_g(t) = F_f \frac{1}{m_1}\sin(w_f t) = F_f \frac{w_f^2}{k_1}\sin(w_f t) \tag{54}$$

where $\ddot{u}_g(t)$ is the ground acceleration, F_f denotes the acceleration amplitude, w_f is the load angular frequency (which is identical to the building's natural angular frequency), and k_1 represents the approximate stiffness of the SDOF system. k_1 can be easily calculated using the perpendicular stiffness of the columns. The response of the building by assuming its behavior as a single-degree-of-freedom system is represented by:

$$u_1(t) = -\frac{F_f}{2k_1}\left[\exp(-\zeta w_f t)\left(\frac{1}{\zeta}\cos\left(w_f\sqrt{1-\zeta^2}t\right) + w_f\sin(w_\zeta t)\right) - \frac{1}{\zeta}\cos(w_f t)\right] \tag{55}$$

where ζ is the damping ratio coefficient and has been taken as 0.05.

The response in Figure 4 shows that the results with second-order elements (traditional elements) are similar to those obtained by Seismostruct and OpenSeesPy, which validate the basis of the numerical method. It is not easy to determine the actual result because Equation 555 is for an SDOF simplified system, while the employed software programs apply different approaches to solve the same problem. Therefore, the coefficient of variation (COV) is used to evaluate the reliability of the findings. The obtained COV of the amplitudes is 0.029, which implies a very low dispersion and high reliability.

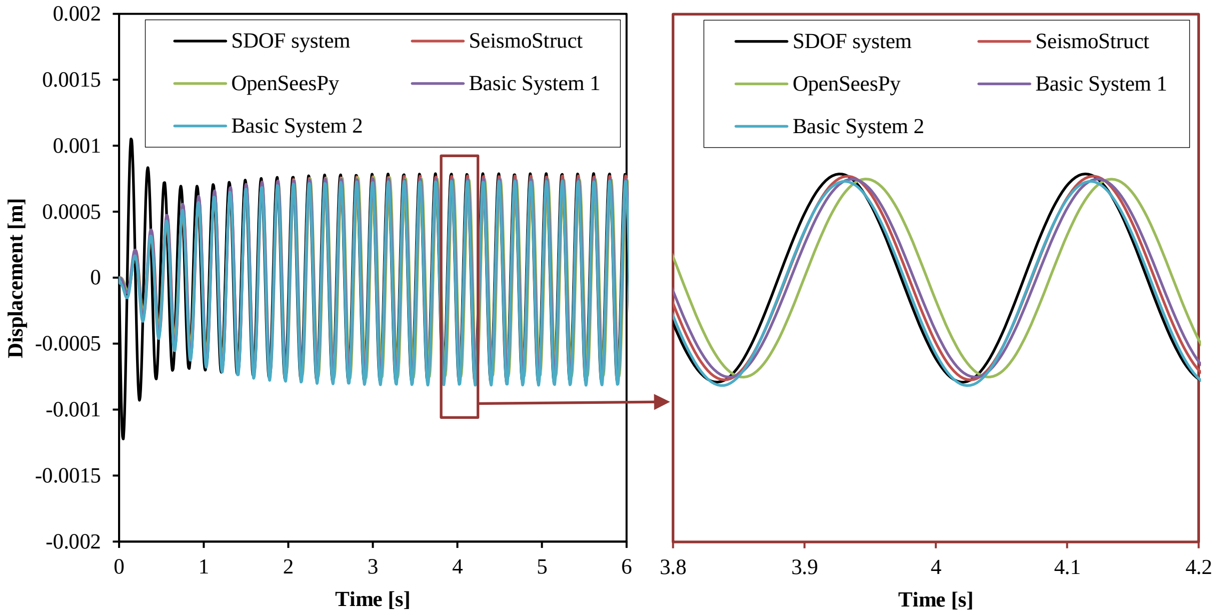

Figure 4. A typical high-order beam-column finite element

Afterward, the order is increased for each element by two since two degrees of freedom arise for each additional node. In Figure 5, it can be appreciated that after the 10th-order elements (four additional nodes in each element), the quality of the result starts to decrease. The truncation and round-off errors are displayed in Figure 6 using Equations 22 and 26 for this building. The errors coincide with the response of the structure, which validates the necessity of selecting the most influential elements to increase their order with the p-adaptive method.

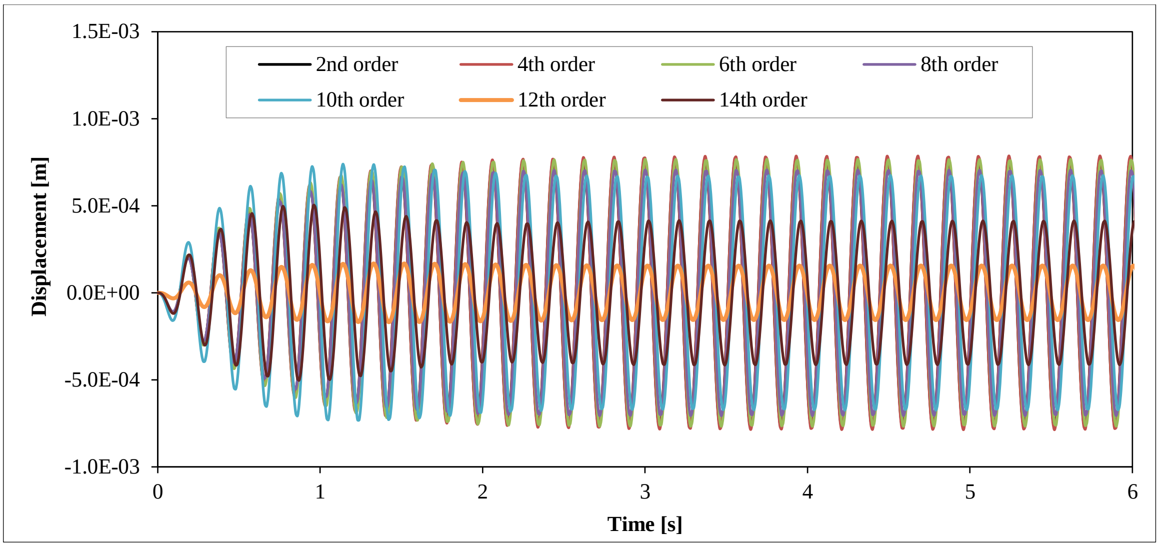

Figure 5. Comparison of different shape function orders

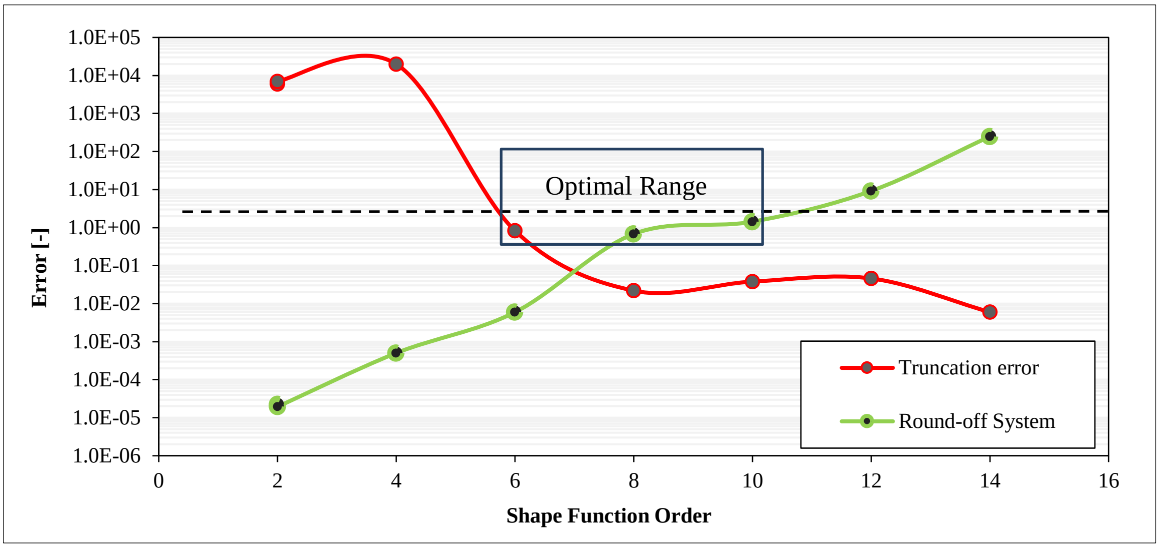

Figure 6. Truncation and round-off error of one-degree-of-freedom building subjected to a sinusoidal load

Three nodes are added to the beams after using the *p*-adaptive method and controlling the round-off error. The building's responses before and after using the *p*-adaptive method are very similar to those expected; see Figure 7. The COV obtained is only 0.03, which supports the validation of the formulation proposed.

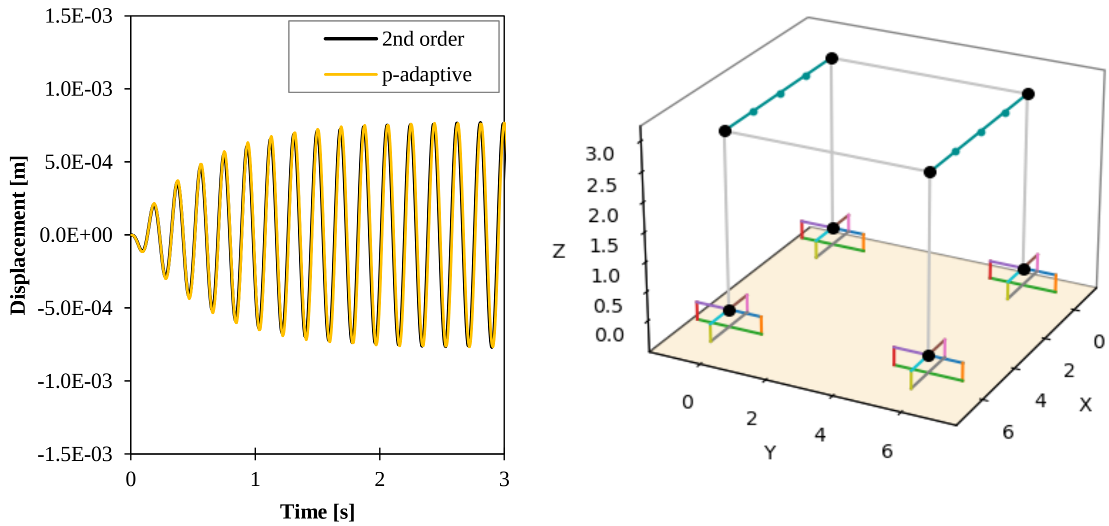

Figure 7. Response of structure before and after using the p-adaptive method (left) and additional nodes in elements (right)

3.2. Validation of the Strategy to Reduce the Numerical Method Error

The proposed strategy, based on an adaptive structural complexity, allows the completion of the structural analysis using a low tolerance error for the numerical method used. The following example shows the utility of this strategy. The building proposed for this validation is small enough to obtain results relatively quickly and large enough to get to a complexity that shows the abovementioned problems. The used building is a 3-floor plan-regular structure with three spans made of reinforced concrete with square columns of 0.4×0.4 m^2 and rectangular beams of 0.3×0.3 m^2. The columns' reinforcement is $16\phi14$, and the beams' upper and lower reinforcement is $4\phi14$ each. The damping ratio coefficient used was 0.05, and rigid diaphragms were considered. The shape function order of the upper columns was increased (without the p-adaptive method) since the vibration of the upper floor can cause convergence problems, which is an extreme case. The structural analysis is linear, yet a large ground motion acceleration is used to provoke instability. Furthermore, rigid diaphragms are used for each floor, and a weight of 7.5 KN/m is added to the element's self-weight. The additional weight is considered to be the floor and walls. The round-off error resulted in 1.93, which is accepted to demonstrate the strategy performance. The maximum truncation error was lower than in the above-studied case; it was 3.96 and was reduced to 0.021. The building dimensions and high-order elements can be seen in Figure 8.

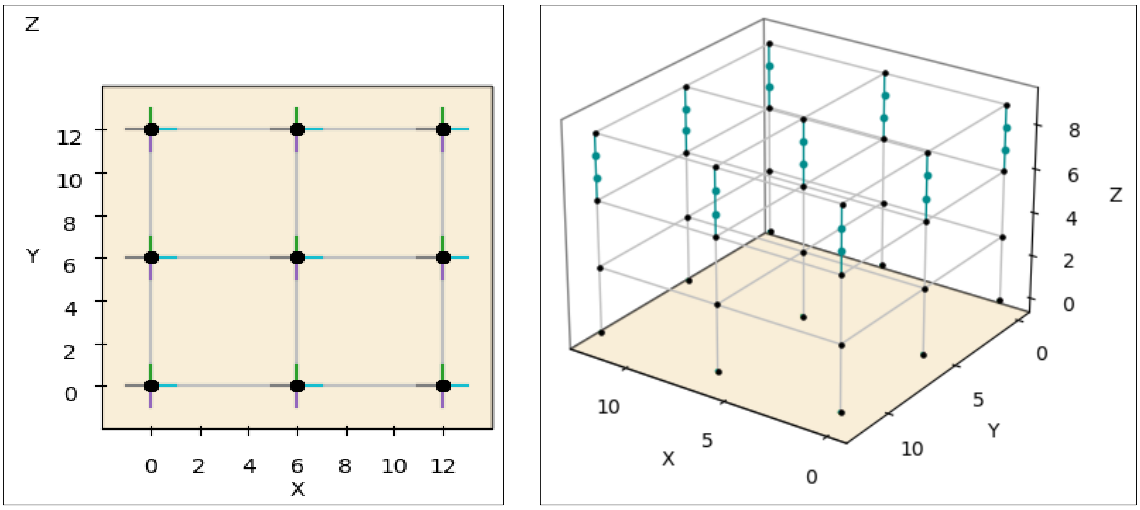

(a) (b)

Figure 8. (a) Plan view and (b) perspective view of the regular building to evaluate the proposed strategy

Figure 9 shows that the results are similar without differences in the response peaks. However, the analysis without the strategy did not converge after the instant 3.84 s. The problem can be found in the analysis of the angular DOF of the top floor, see Figure 10. It must be noted that the rotational displacement in this DOF is nearly zero, and in the "high-order elements, no strategy" model, its behavior presented divergence. The building responses obtained from the p-adaptive method were found after applying the filtered mass matrix proposed in the strategy (model "high-order elements, strategy").

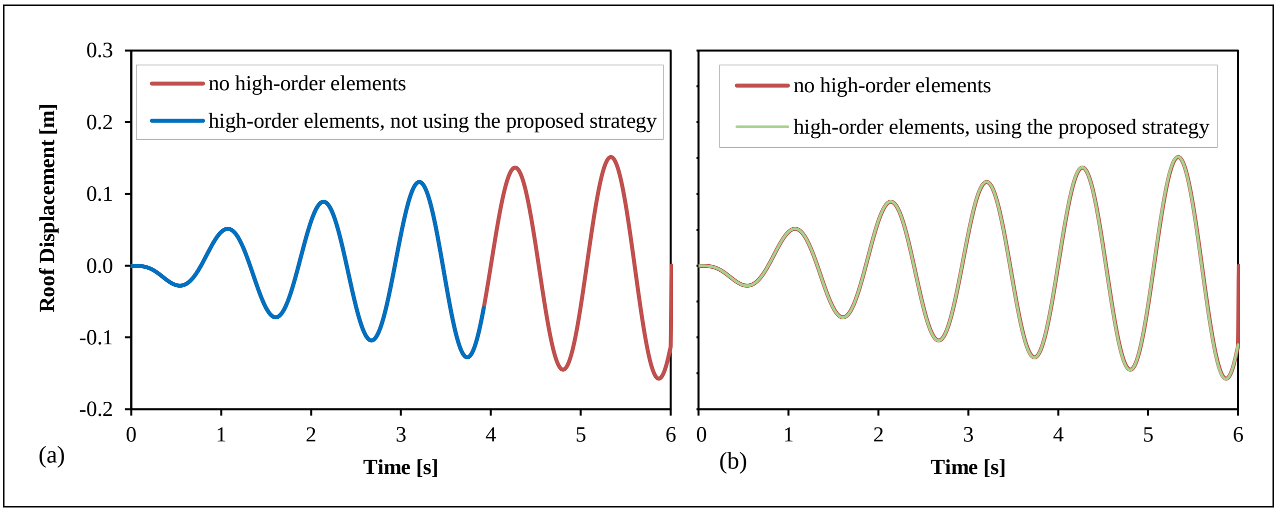

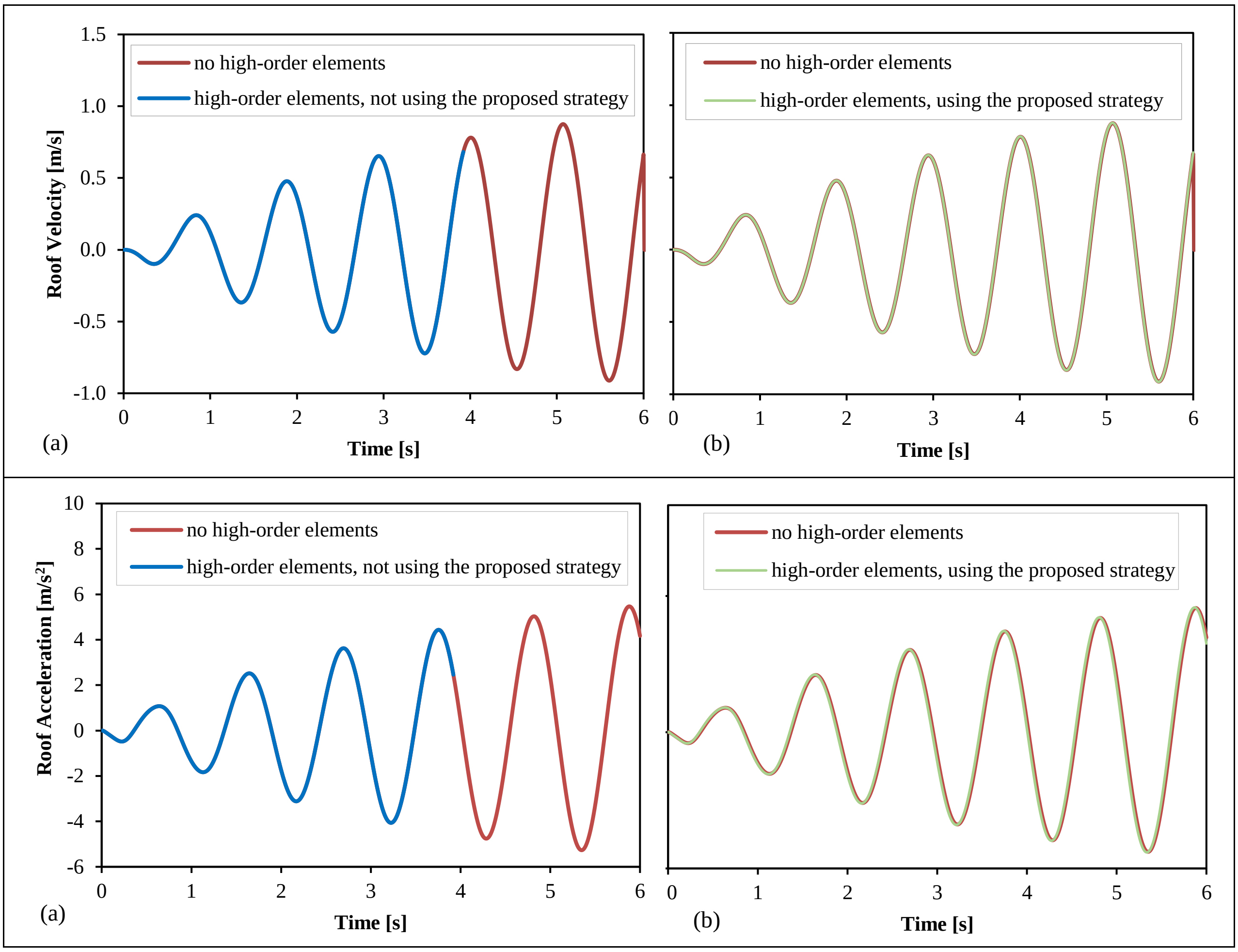

Figure 9. Displacement, velocity, and acceleration responses on the top of the building (a) without and (b) with using the proposed strategy

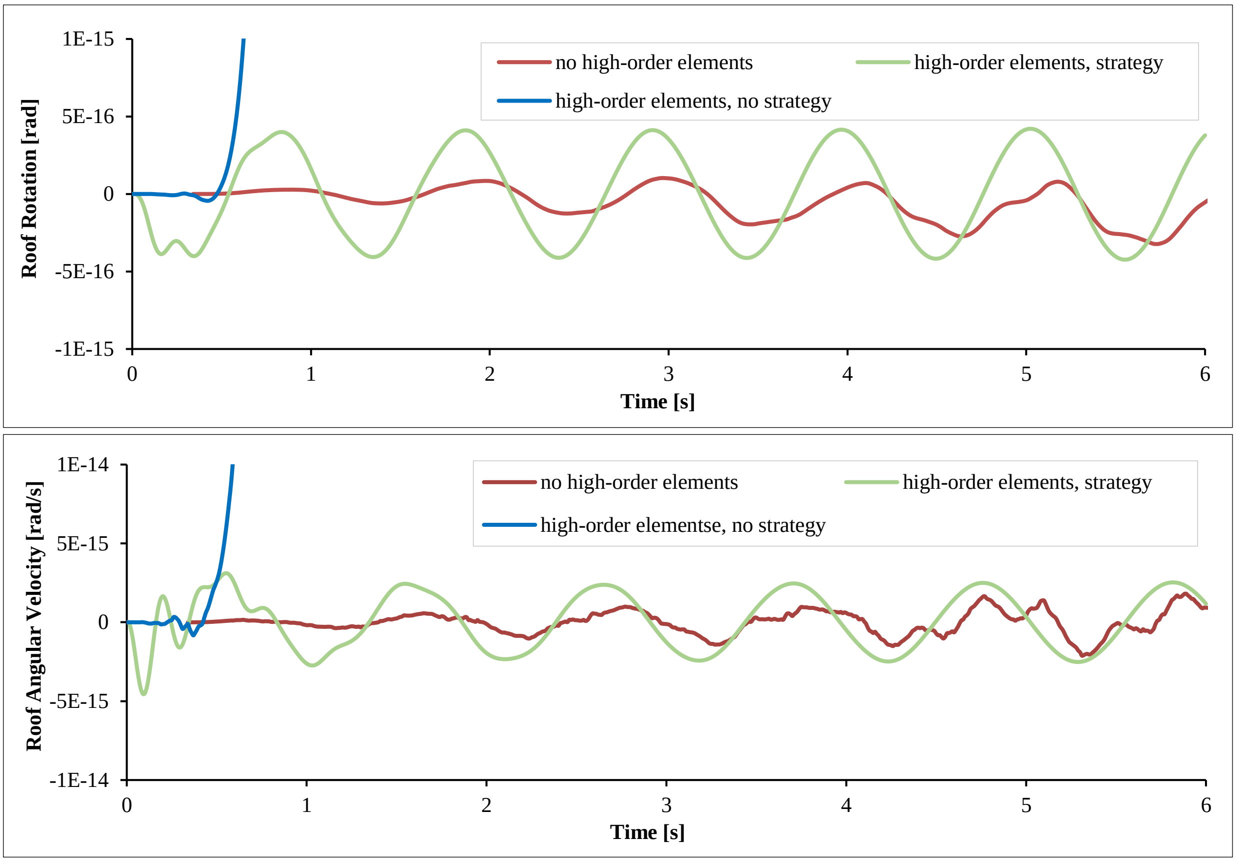

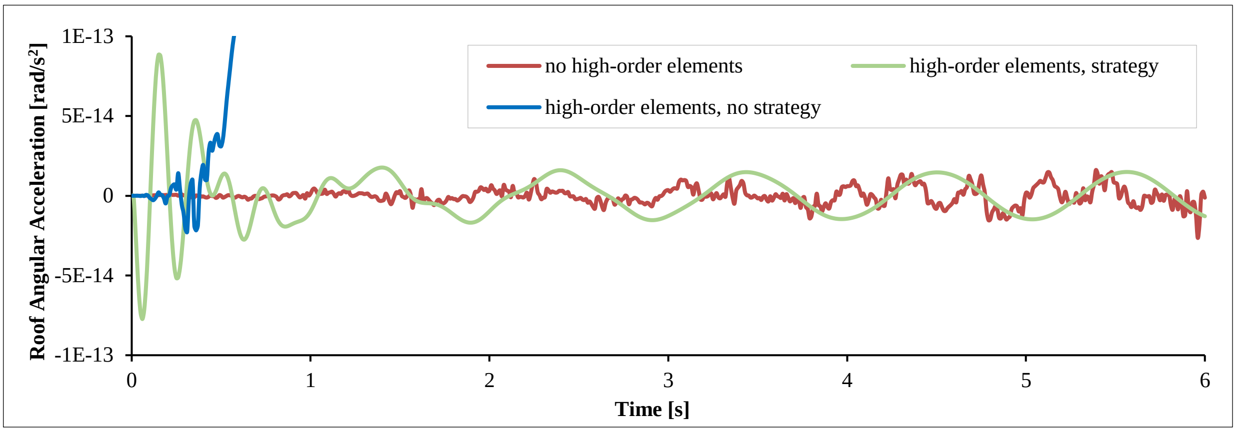

Figure 10. Rotation, angular velocity, and angular acceleration responses on the top of the building

3.3. Validation with an Actual Experiment Structure

The p-adaptive method will help obtain more accurate results in more complex structures, where significant differences could occur between using this method and not using it. Theoretically, the proposed formulation will provide more accurate results, yet it is difficult to prove it to real buildings since no available data exists. However, a small experiment was led to motivate more future large-scale experiments. This test consists of a small three-floor steel structure (17×30×51 cm) (see Figure 11-a) that was analyzed on a one-degree-of-freedom shaking table (see Figure 11-b). The shaking table has a base area of 70×30 cm, which works with two 500 W motors for the experiments. One-dimensional sinusoidal vibration was used. The sinusoidal movement has a frequency of 3.19 Hz with an amplitude of 3.92 m/s^2. The elements were welded and included a plate that simulated rigid slabs. Its footings were plates bolded to the shaking table. Accelerometers of the types ASC (measuring range up to $\pm$50 g) and ADXL345 (measuring range up to $\pm$16 g). In addition, a digital camera type Canon EOS 2000D was used to take photos with a resolution of 2 megapixels (MP) at 25 frames per second (fps) for comparing the results with the digital image correlation (DIC) method; more details of this experiment can be found on Pankrath et al. [57]. The exact ground-building movement (GBM) was used in the building computational models. Moreover, the GBM was subtracted from floor responses to obtain results relative to the building base, such as the structural analysis responses. The experiment building had a natural period of 0.44 s and a damping ratio coefficient of 0.098, obtained after analyzing its free vibration response.

(a)

(b)

(c)

Figure 11. Experiment with (a) a three-floor structure, (b) the DIC methodology process, and (c) the shaking table used

The building tested was made of steel. After laboratory tests on the steel material, the following properties were determined: the steel modulus of elasticity is 203.89 GPa, the yield tension point is 253.11 MPa, and the ultimate tension point is 407.78 MPa. The elements are rectangular plates of 0.012×0.003 m sections for both beams and columns. Moreover, a weight of 2.39 kN/m^2 was added to each floor through a steel plate. The building is 0.30 m on the X-direction, 0.17 m on the Y-direction, and each column size is 0.17 m (see Figure 12). The acceleration is transmitted to the structure through a ground motion in the X-direction, and a linear analysis was performed with the mentioned parameters. The truncation and round-off errors after increasing the order of all the elements are displayed in Figure 13. The truncation and round-off errors are shown in Figure 13 after applying the proposed methods. The refined structure grid after employing the p-adaptive method is presented in Figure 12. The refined elements are represented with additional nodes (two orders are added with each extra node).

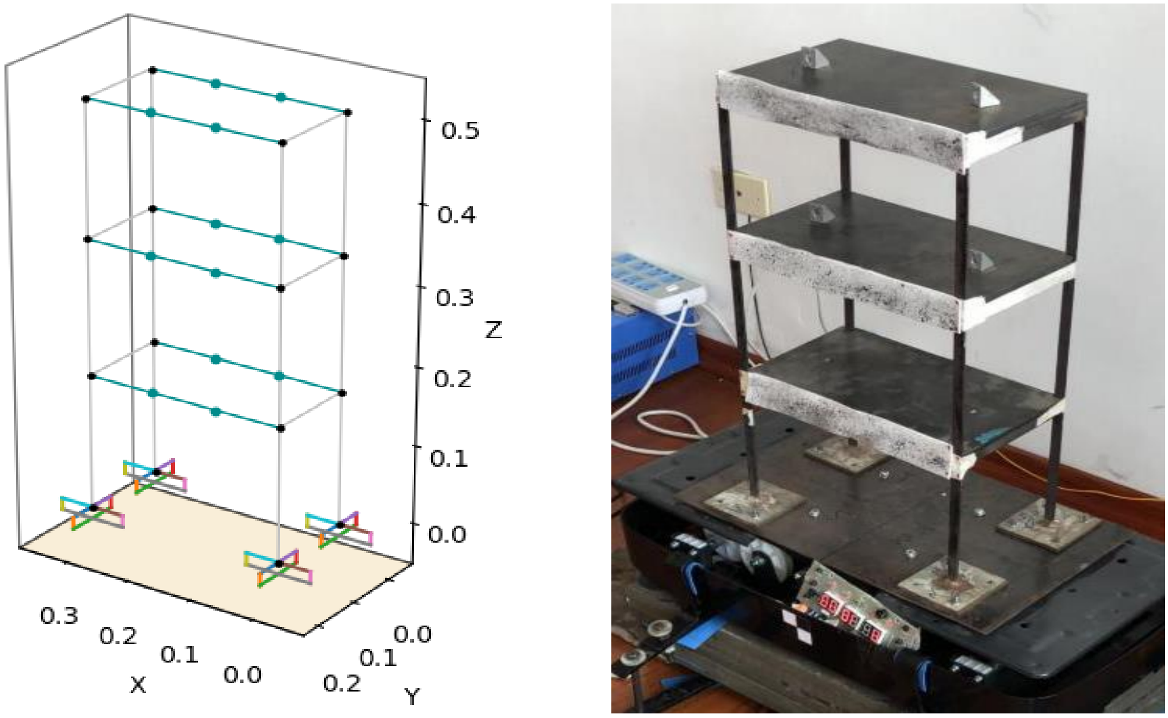

Figure 12. High-order elements in the building experiment. Small circles indicate additional nodes

Figure 13. Truncation and round-off error of experiment building subjected to a sinusoidal load

The structure's displacement of each floor from the experimental building, the traditional analysis, the OpenSees analysis, and the p-adaptive analysis are shown in Figures 14 to 16. From these comparisons, differences in the amplitude responses can be appreciated. Thus, the Euler norm is obtained between the distances of the experimental building ($\boldsymbol{u}_{experiment}$) and the structural analyses ($\boldsymbol{u}_{analysis}$) in each instant. The scaling laws for dynamic models are factors that affect the structure responses, e.g., the displacements are directly proportional to the ratio of model-to-prototype length [58-60]. Therefore, the relative error is the same for the scale model and an actual building since those factors can be simplified (see Equation 67). Thus, the norm results are normalized by the Euler norm of the experimental building displacements as follows:

$$error = \frac{\|\boldsymbol{u}_{experiment} - \boldsymbol{u}_{analysis}\|}{\|\boldsymbol{u}_{experiment}\|} \tag{67}$$

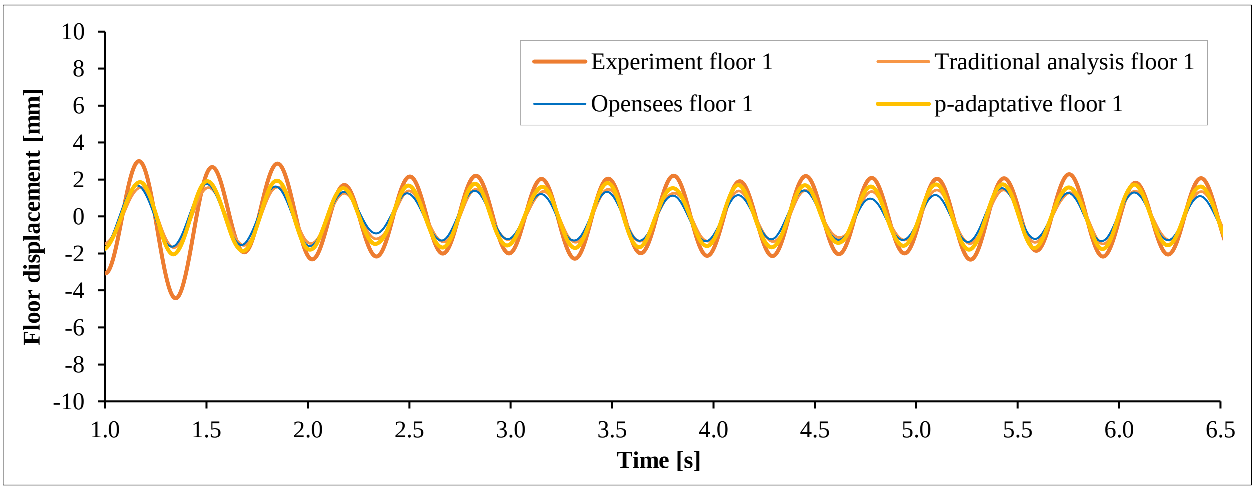

Figure 14. Experimental building floor 1 displacement and structural analyses responses

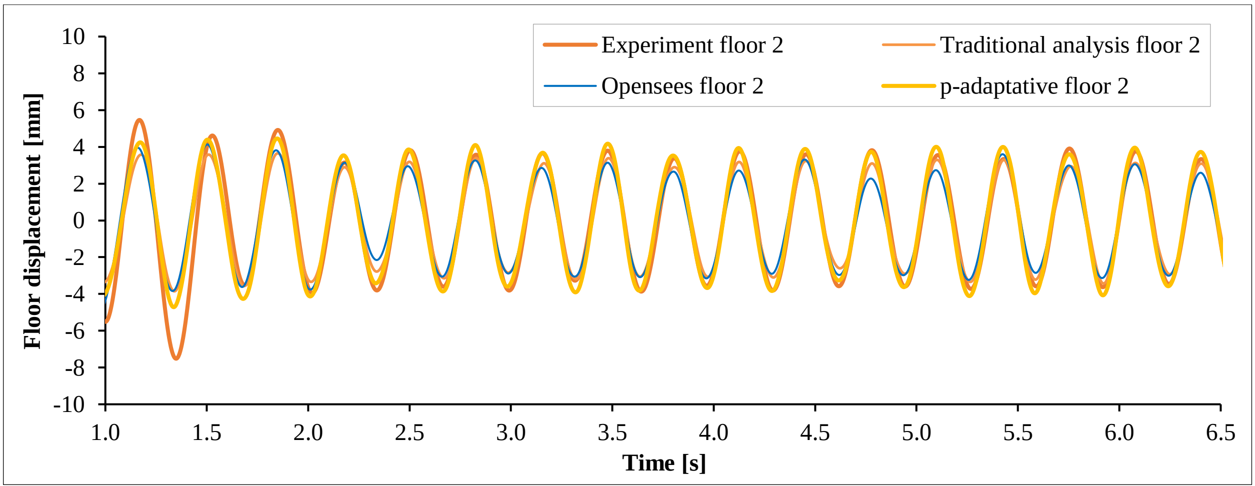

Figure 15. Experimental building floor 2 displacement and structural analyses responses

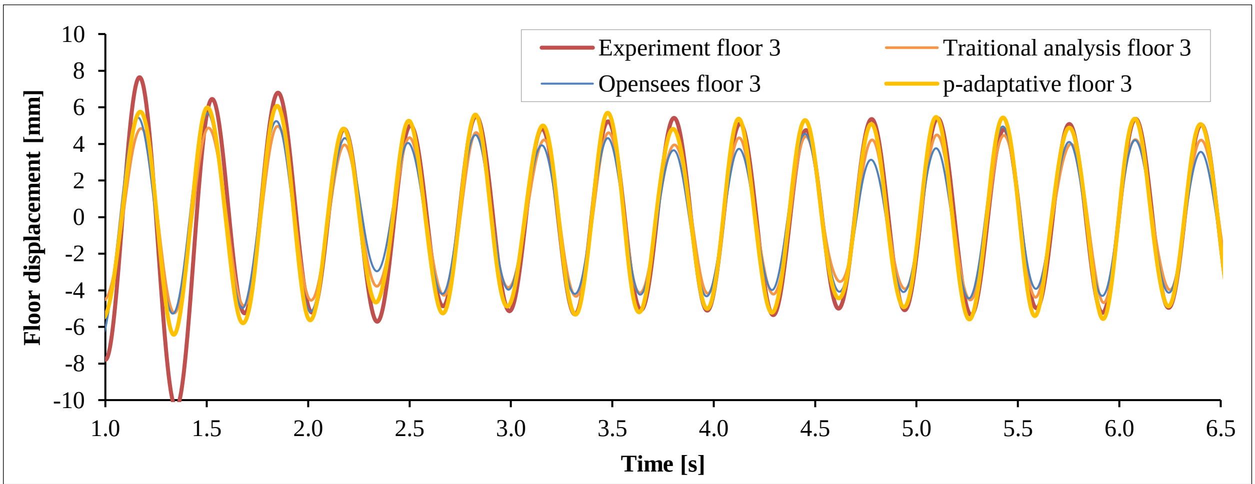

Figure 16. Experimental building floor 3 displacement and structural analyses responses

In Floor 1, the displacement of the experiment compared to the traditional analysis (second-order elements) is 28.69%, compared to OpenSees results of 31.97%, and compared to p-adaptive analysis results of 22.49%. In Floor 2, the displacement of the experiment compared to the traditional analysis is 22.02%, compared to OpenSees 28.44%, and compared to p-adaptive analysis 17.98%. Finally, the difference between the Floor 3 displacements of the experiment and the traditional analysis is 18.43%, OpenSees is 22.94%, and p-adaptive analysis is 12.51%. In summary, the total error for the traditional analysis is 23.05%; for the OpenSees results, it is 27.79%; and for the p-adaptive method, it is 17.66%. Therefore, these differences in results have motivated the analyses performed in the following section to investigate the influence of refinement elements on more realistic buildings.

4. Numerical Examples using the p-adaptive Method

In the following examples, the influence of the p-adaptive method on massive structures will be tested. Equations 22 and 26, stated for the p-adaptive method, have been used in the following examples. They are employed while the ground motion records are used to analyze the structures. The Hermitian interpolation is used to fill gaps that appear when additional DOFs are increased when the order of the elements is raised. Moreover, the general algorithm changes the elements between elastic and inelastic analyses [61] according to a limit stated for yielding points following Monti and Petrone [54]. The formulation has been verified with six structures of different complexities, nonlinear behavior, materials, and irregularities. They are presented in Figure 17.

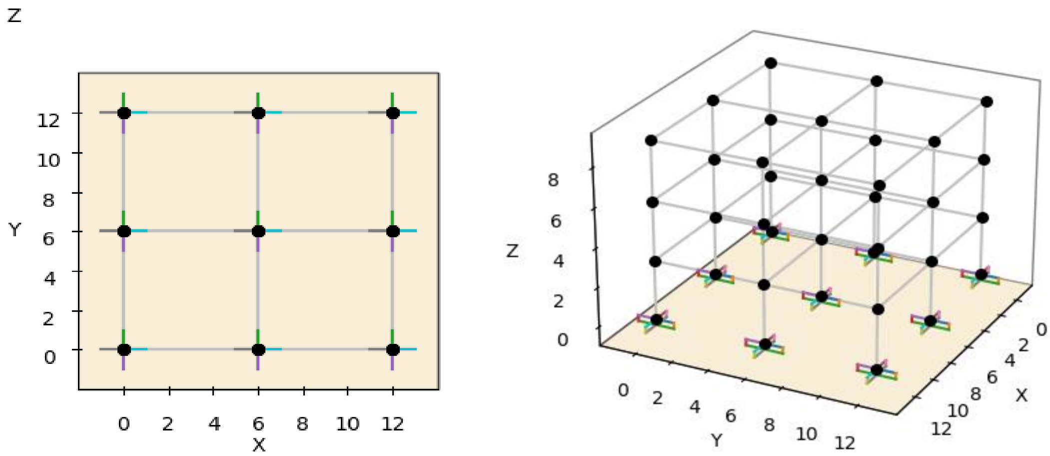

Building 1

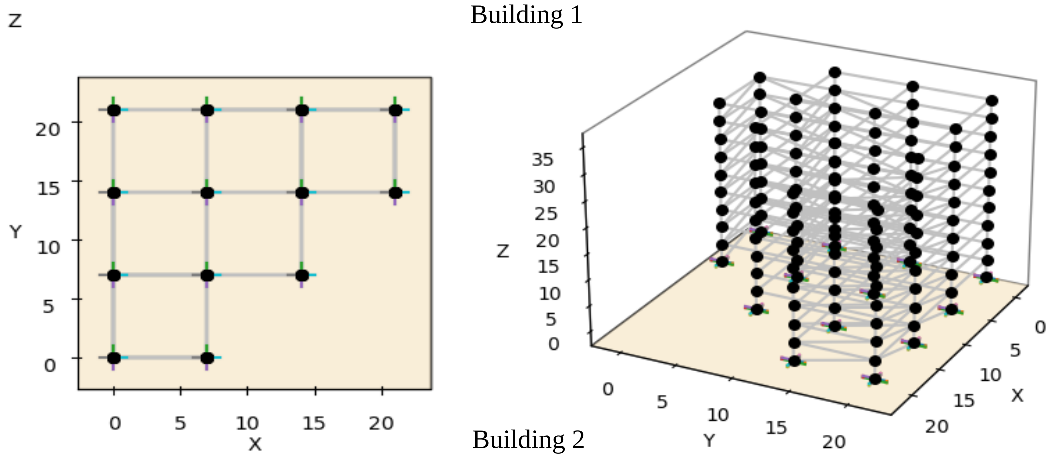

Building 2

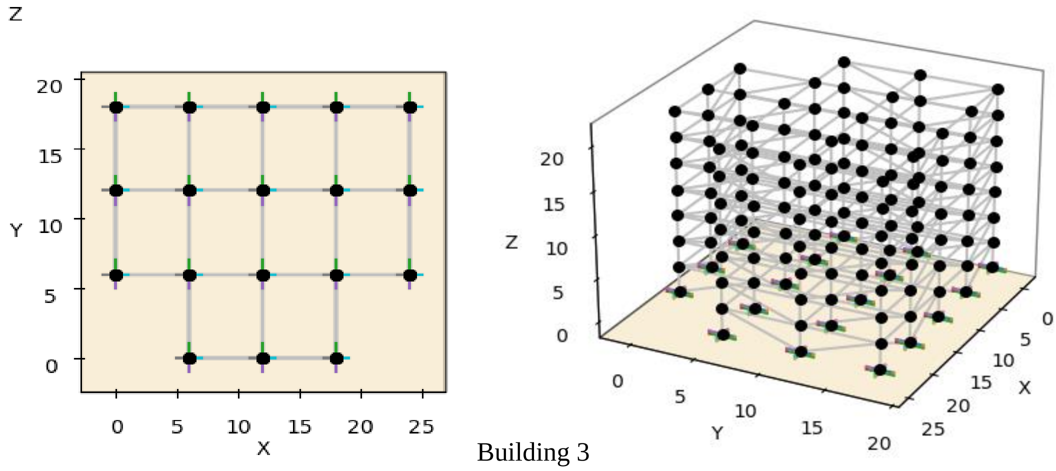

Building 3

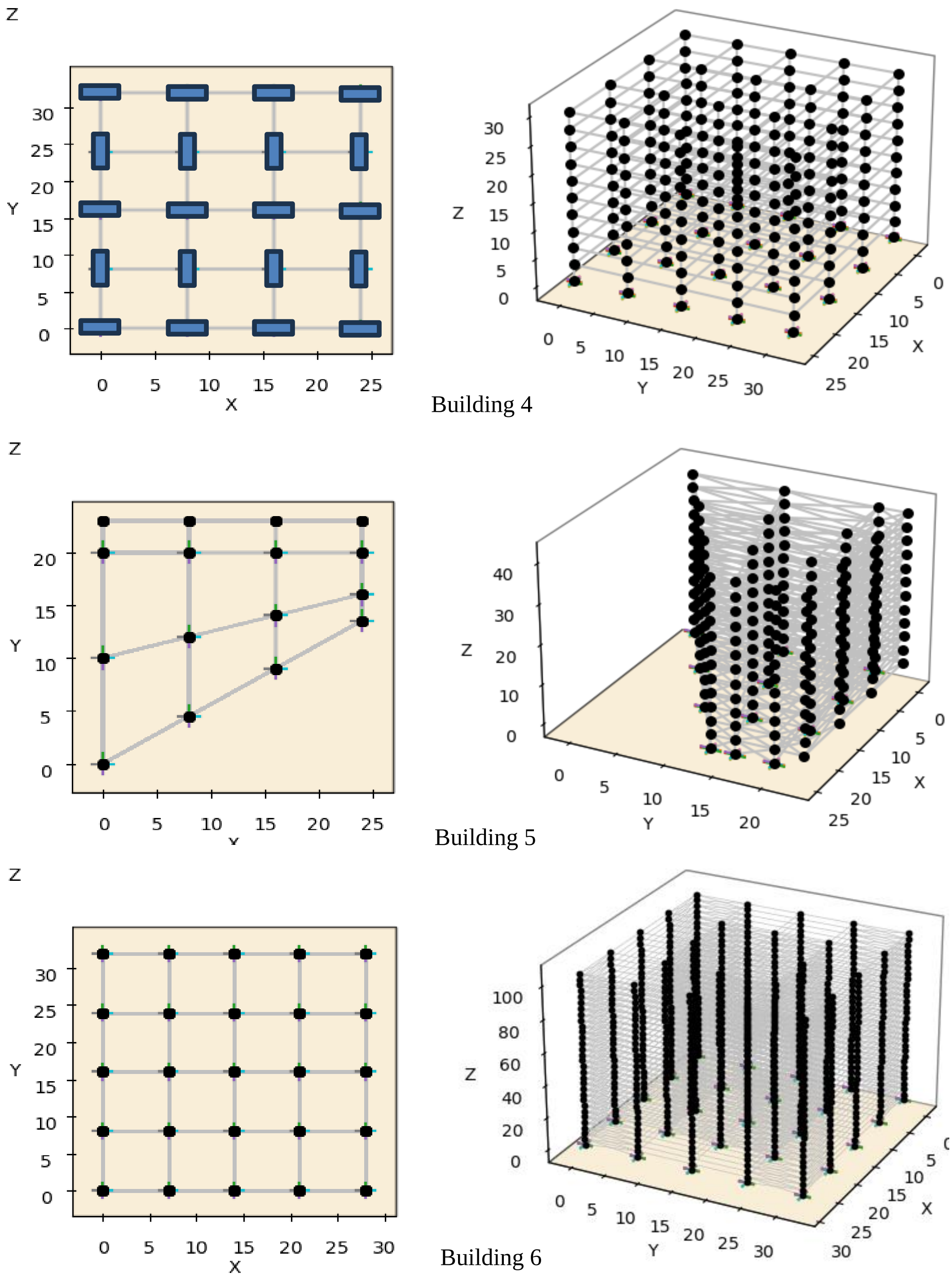

Figure 17. Plan view (left) and perspective view (right) of the buildings analyzed in this study

The buildings are made of concrete using the following properties. The Young modulus of concrete E is 21.5 GPa, its compressive strength f_c is 21 MPa, its specific weight γ is 24 KN/m^3, and the yield strength f_y of rebars is 590 MPa. Moreover, the elements' self-weight and an additional 7.5 KN/m^2 weight are applied. The additional weight involves estimating the slab and wall weights, and it is automatically transferred by the software made from the slabs to the beams as uniform loads using triangular and trapezoidal tributary areas. Additionally, a compression ultimate strain of 0.0035 and a tensile ultimate strain of 0.0003 were used for confined concrete fibers. The ultimate strain used in nonconfined concrete is 0.00105 for a compressive strain and 0.0001 for a tensile strain. An ultimate strain of 0.2 was used for steel fibers. The structures' elements were sized so that some elements go to the nonlinear range for the applied strong ground motion records. The ground motions used are signals from accelerograms of actual earthquakes. Moreover, the matrix calculation of the structural analysis was made using sparse matrices, and the rigid diaphragm criterion was taken for all slabs. Three ground motions were used, and the results are shown according to the building's most unfavorable response. Table 1 presents the properties and special characteristics of the analyzed buildings.

Table 1. Properties and Special Characteristics of the Buildings

Building	No. of Floors	Columns [m^2]	Columns rebars [mm]	Beams [m^2]	Beams rebars [upper = lower][mm]	Special characteristic	Earthquake
1	3	0.40 × 0.40	$16\phi14$ $f_y = 420$ MPa	0.30 × 0.40	$4\phi14$ $f_y = 420$ MPa	-	Tohoku-Japan (2011)
2	10	1.00 × 1.00	$36\phi22$ $f_y = 420$ MPa	0.40 × 0.70	$5\phi22$ $f_y = 420$ MPa	Dampers BRB Core: 0.30 × 0.03 m^2 $f_y = 150$ MPa	Concepción-Chile (2010)
3	7	0.30 × 0.30	$8\phi16$ $f_y = 420$ MPa	0.30 × 0.45	$3\phi16 f_y = 420$MPa	Reinforced concrete braces of 0.30 × 0.30 m^2 using $8\phi16$ at axial, torsional, and bending strength $f_y = 420$ MPa	Concepción-Chile (2010)
4	10	$b_Y = 0.60$ $h_X = 3.00$	$16\phi32$ & $56\phi20$ $f_y = 420$ MPa	0.40 × 0.90	$5\phi20$ $f_y = 420$ MPa	-	El Centro-USA (1940)
		$b_Y = 3.00$ $h_X = 0.60$	$56\phi20$ & $16\phi32$ $f_y = 420$ MPa				
5	12	2.20 × 2.20	$92\phi32$ $f_y = 590$ MPa	0.40 × 0.90	$12\phi32$ $f_y = 590$ MPa	3 m cantilever & fragile masonry of $t = 0.15$ m, modeled as struts: $f_m = 3$ MPa; $E_m = 600 f_m$	Concepción-Chile (2010)
6	30	Floor 1-10: 1.50 × 1.50	$196\phi32$ $f_y = 420$ MPa	0.40 × 0.80	$5\phi25$ $f_y = 420$ MPa	Floor 1-10: Dampers BRB Core: 0.20 × 0.02 m^2 $f_y = 250$ MPa	Concepción-Chile (2010)
		F. 11-20: 1.40 × 1.40	$180\phi32$ $f_y = 420$ MPa			F. 11-20: Dampers BRB Core: 0.10 × 0.01 m^2 $f_y = 250$ MPa	
		F. 21-30: 1.30 × 1.30	$164\phi32$ $f_y = 420$ MPa			F. 21-30: Dampers BRB Core: 0.20 × 0.0125 m^2 $f_y = 250$ MPa	

The ground accelerations used are Concepción-Chile (2010), Tohoku-Japan (2011), and El Centro-USA (1940), which are shown in Figure 18. The peak ground acceleration is 0.35 g for the Concepción, 0.96 g for the Tohoku, and 0.28 g for the El Centro. Furthermore, an essential parameter for the building characteristics is the predominant frequency. The frequencies obtained from a Fast Fourier procedure of the Concepción ground motion are between 0.30 Hz and 1.95 Hz, the Tohoku motion is 4.30 Hz, and the El Centro motion is 4.69 Hz. The signals have been filtered, and their baseline were corrected.

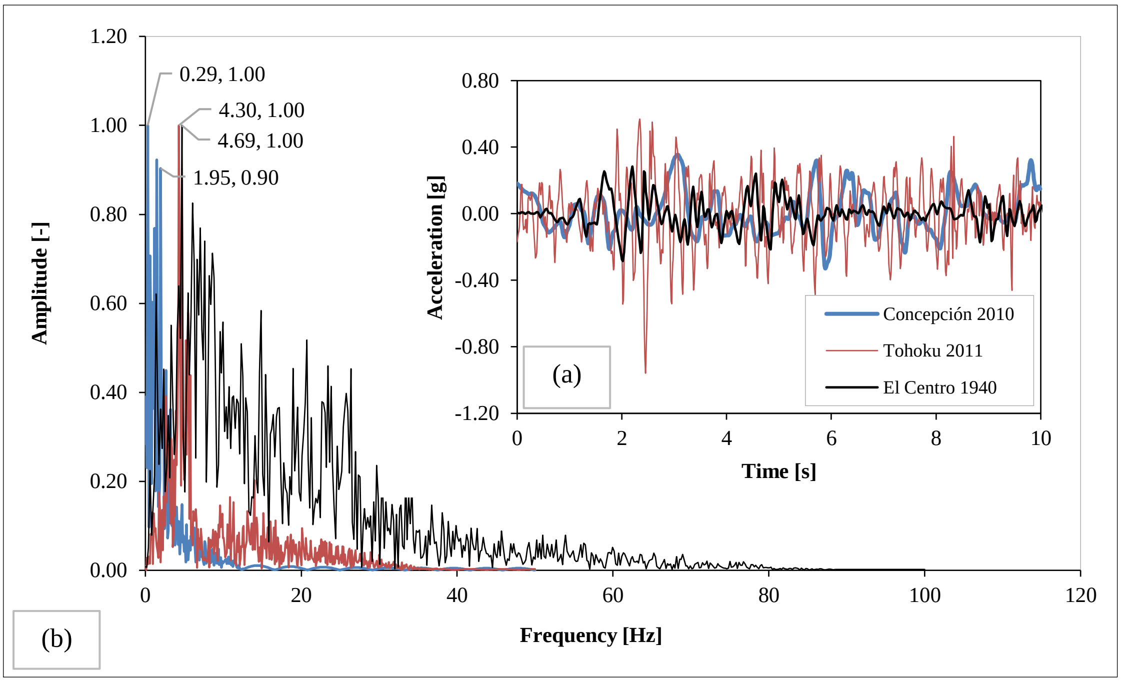

Figure 18. (a) Time-history and (b) frequency spectrum of Concepción 2010, Tohoku 2011, and El Centro 1940 ground motions

5. Results of Nonlinear Analyses of Buildings

The first evaluated analyses are the models that do not use the p-adaptive method but use the strategy proposed. It is labeled "No p-adaptive, strategy" for the comparisons. The second analysis is the theoretically more accurate structure. It is the analysis using the p-adaptive method for each two time-history analysis instant before some element has yielded to avoid convergence problems, as mentioned before. This analysis is the benchmark labeled "p-adaptive, strategy" for comparison purposes. Finally, the third analysis was carried out in OpenSees. It uses the same geometric and material characteristics to provide an additional reference for monitoring the developed software since OpenSees has already been validated in some studies [62]. This analysis is a no p-adaptive nonlinear time-history procedure, and it is labeled as "OpenSees." It is also important to mention that the strategy used in the own-made software allowed to set an error tolerance of $1E-10$, and the error tolerance that worked in OpenSees better was a value of $1E-3$. The results analyzed are (1) the roof displacements, since they represent the influential vibration modes, and (2) the elements' performance, measured by evaluating the elements that have reached the yielding (colored in green) or breaking points (colored in red).

The truncation error was reduced with the equations stated for the p-adaptive method, and the number of high-order elements was limited by the round-off error. As a result, the high-order elements were calculated in real-time in the time-history procedure, and they are represented with cyan circles that symbolize additional internal nodes, as shown in Figure 19. Since the round-off error rises rapidly in large structures, only two additional nodes resulted in an increase in the indicated elements, which means four order elements. The results for the time versus the roof displacement of the buildings are shown in Figure 20, and the amount by which the errors were reduced is presented in Table 2.

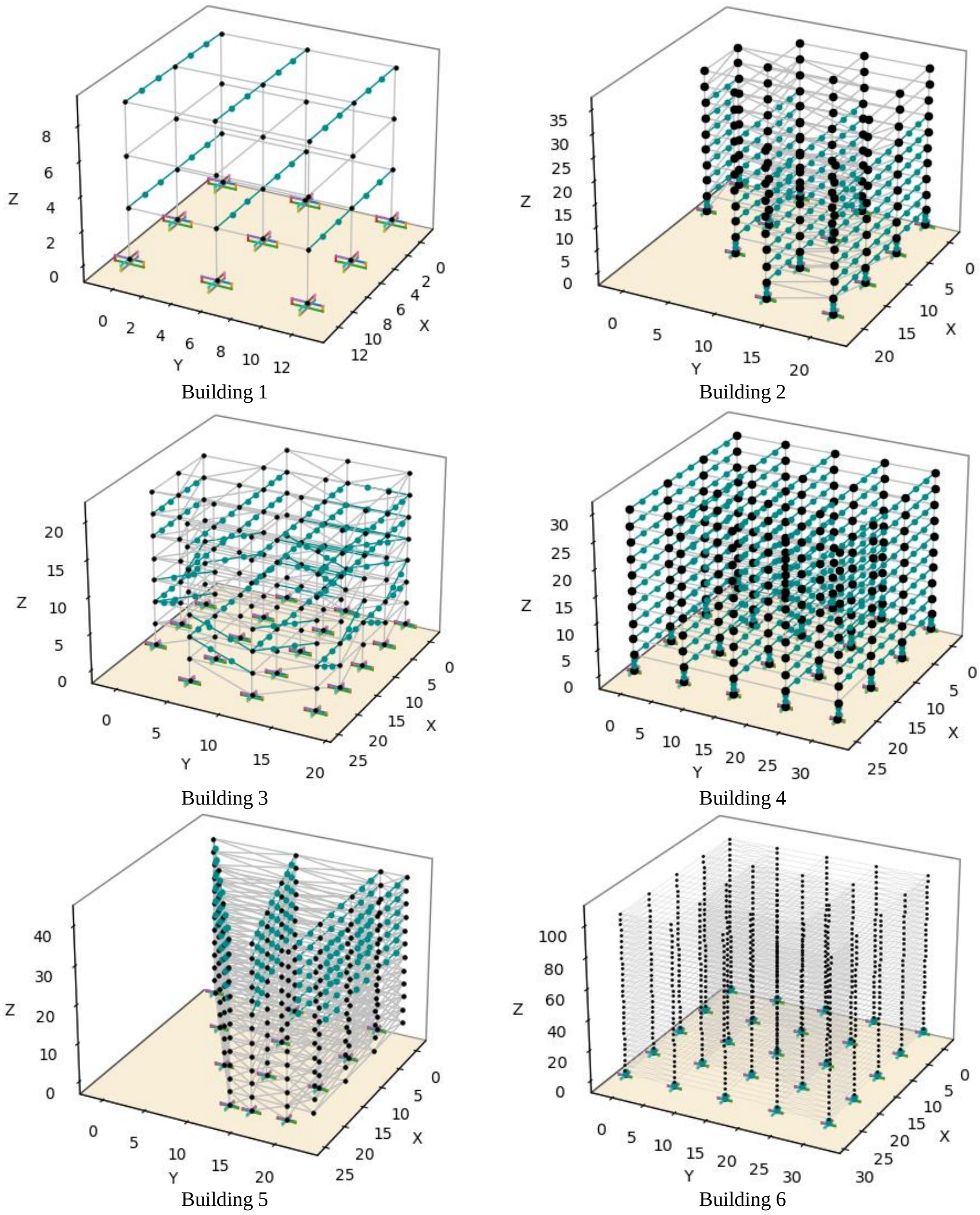

Figure 19. High-order elements in the buildings. Small circles indicate additional nodes

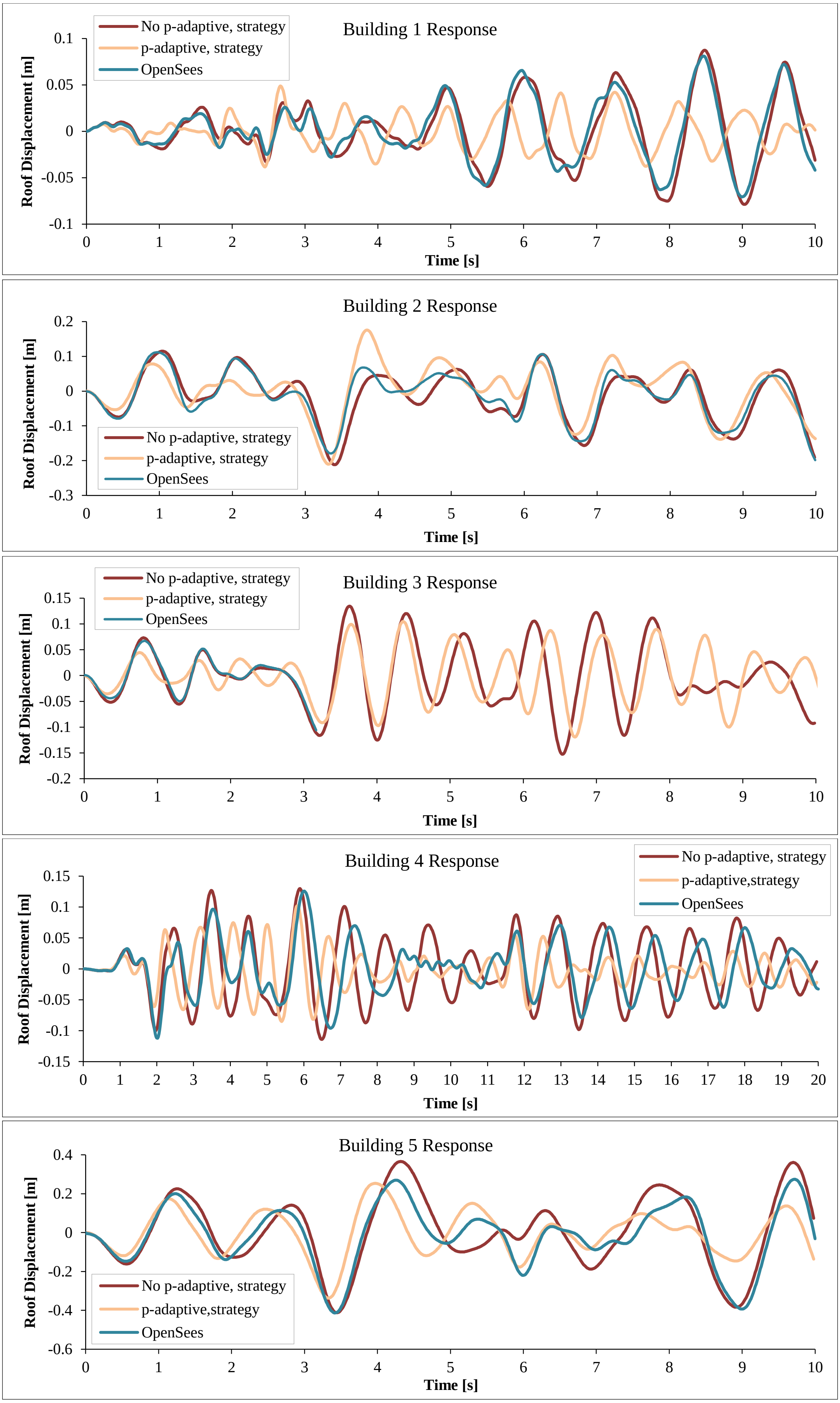
Building 1 Response
No p-adaptive, strategy
p-adaptive, strategy
OpenSees
Roof Displacement [m]
Time [s]
Building 2 Response
No p-adaptive, strategy
p-adaptive, strategy
OpenSees
Roof Displacement [m]
Time [s]
Building 3 Response
No p-adaptive, strategy
p-adaptive, strategy
OpenSees
Roof Displacement [m]
Time [s]
Building 4 Response
No p-adaptive, strategy
p-adaptive,strategy
OpenSees
Roof Displacement [m]
Time [s]
Building 5 Response
No p-adaptive, strategy
p-adaptive,strategy
OpenSees
Roof Displacement [m]
Time [s]

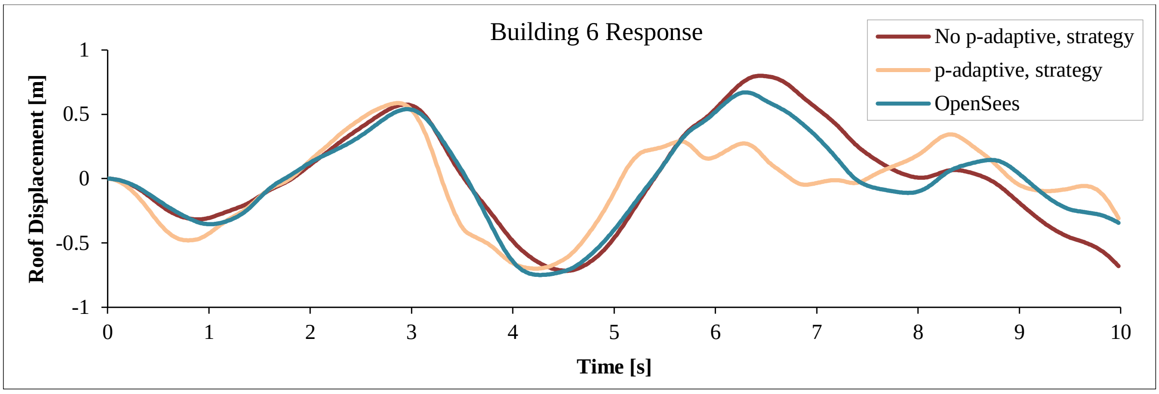

Figure 20. Comparison of the buildings' responses among analyses with the p-adaptive method, without the p-adaptive method, and OpenSees

Table 2. The errors before and after applying the proposed formulation

Building	Truncation error before applying the *p*-adaptive method	Truncation error after applying the *p*-adaptive method	Round-off error before applying the *p*-adaptive method	Round-off error after applying the *p*-adaptive method
1	3.01	0.0305	0.00082	0.0025
2	6.48	0.9291	0.01561	0.0222
3	5.17	0.7913	0.00219	0.2057
4	4.06	0.3530	0.22017	0.3719
5	8.04	0.3647	0.20122	0.2266
6	1.94	0.4752	2.37703	2.5852

In general terms, the similitudes between the results of the software made for this study without using the *p*-adaptive method and OpenSees are notorious in Figure 20. It is worth mentioning that the response of Building 3 could not be obtained with OpenSees for convergence problems. In more detail, the prominent frequency responses between "*p*-adaptive, strategy" and OpenSees in spectra of Fourier in Figure 21 are the same in all the cases. The amplitudes in the most important secondary frequencies vary by 10% in Building 2, 72% in Building 4, and 33% in Building 5. There are also some differences in the peak displacement responses (see Figure 20): 8% in Building 1, 7% in Building 2, 3% in Building 4, 0.2% in Building 5, and 6.7% in Building 6. These variations might have occurred due to the dissimilitudes between the mathematical and computation models and the error tolerance. For example, the corotational model used for OpenSees consists of a flexibility-matrix-based basic system. However, a different basic system was used in this work (see Figure 1), which allowed high-order elements for the subsequent *p*-adaptive method. The differences in results for the basic system matrices can occur since flexibility formulations often use secant stiffness approaches compared to tangent stiffness methods [63]. It can be concluded that the results from the software produced for this work are reliable since the most prominent frequency responses are the same, and the differences from the peak displacements do not make a significant gap.

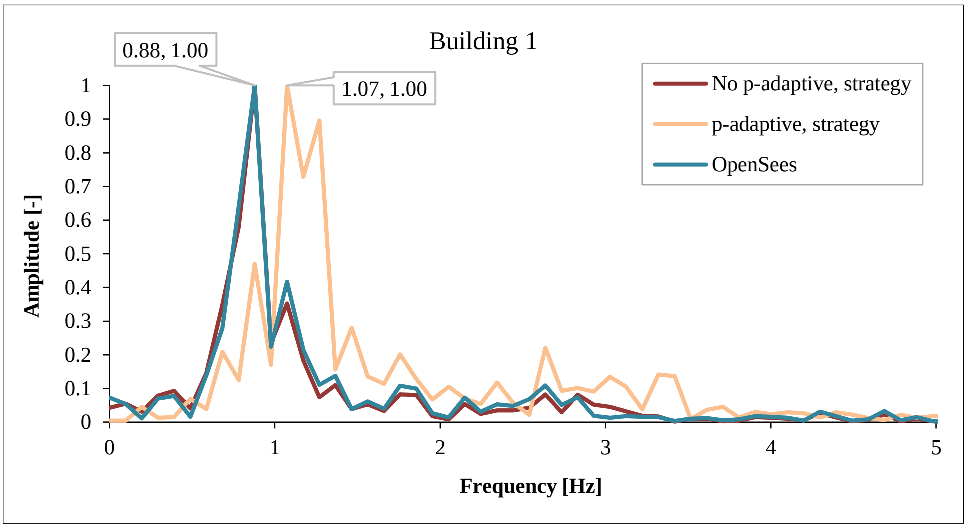

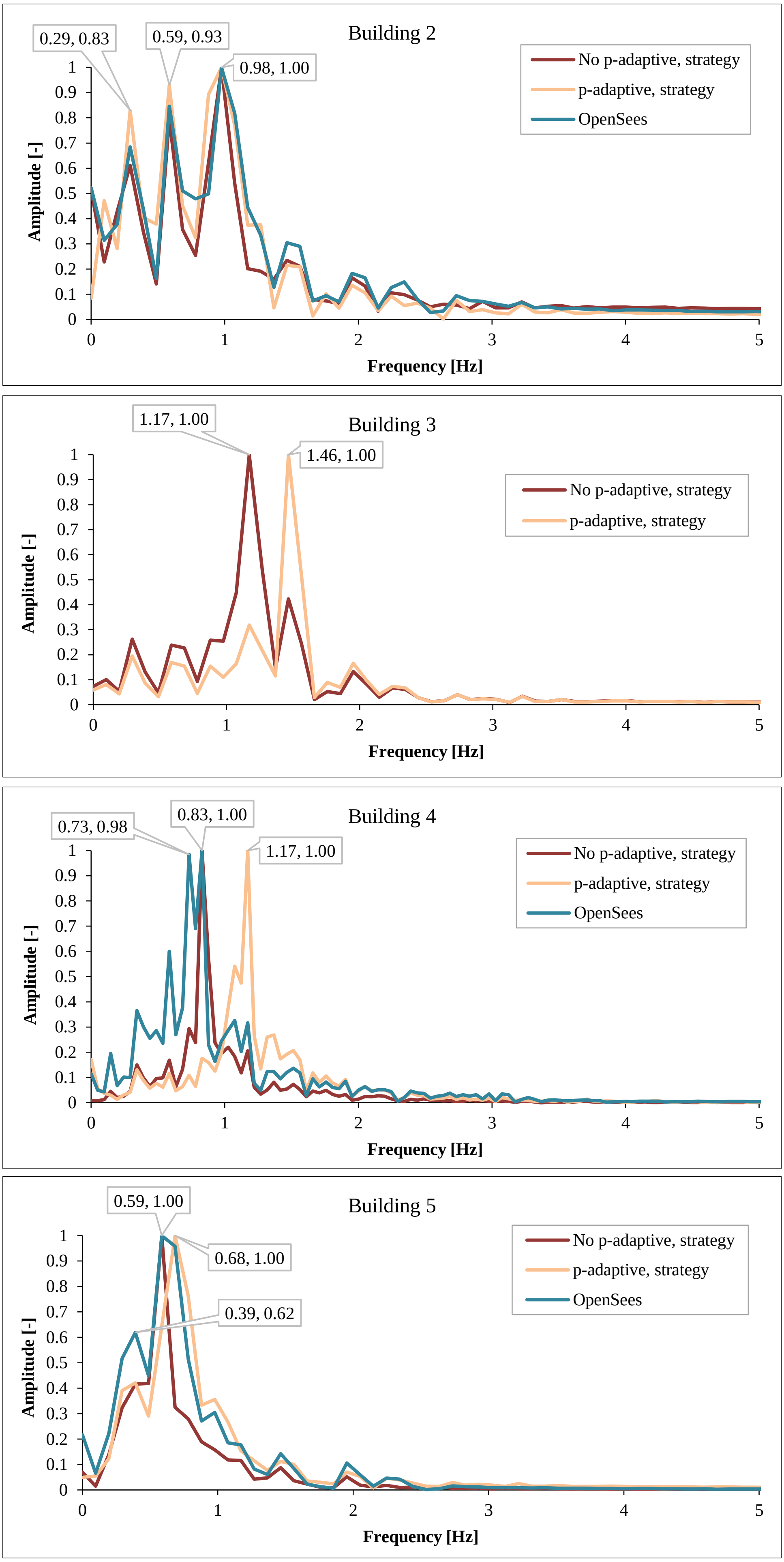
Building 2
0.29, 0.83
0.59, 0.93
0.98, 1.00
No p-adaptive, strategy
p-adaptive, strategy
OpenSees
Amplitude [-]
Frequency [Hz]
Building 3
1.17, 1.00
1.46, 1.00
No p-adaptive, strategy
p-adaptive, strategy
Amplitude [-]
Frequency [Hz]
Building 4
0.73, 0.98
0.83, 1.00
1.17, 1.00
No p-adaptive, strategy
p-adaptive, strategy
OpenSees
Amplitude [-]
Frequency [Hz]
Building 5
0.59, 1.00
0.68, 1.00
0.39, 0.62
No p-adaptive, strategy
p-adaptive, strategy
OpenSees
Amplitude [-]
Frequency [Hz]

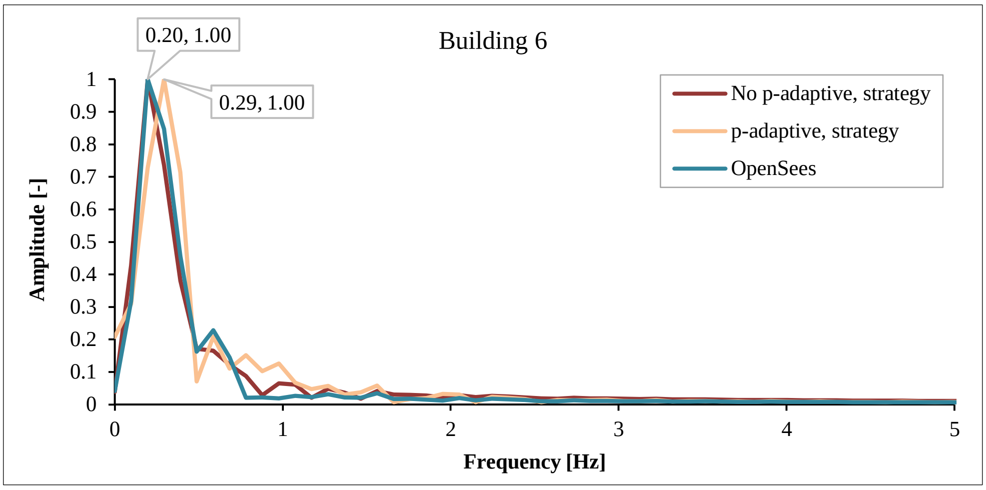

Figure 21. Comparison of the frequency responses in the frequency spectra of Fourier

The contrast between the use of the p-adaptive method is easily noticed in the results of Figure 20. Numerically, these differences can be extracted from the frequency spectra of Fourier in Figure 21. Thus, the error in the most prominent frequencies between using the p-adaptive method and not using it are 25% for Building 1, 0% for Building 2, 20% for Building 3, 29% for Building 4, 14% for Building 5, and 50% for Building 6. The errors for the peak displacement responses are 63% for Building 1, 0.8% for Building 2, 28% for Building 3, 27% for Building 4, 22% for Building 5, and 56% for Building 6. The significant variation in using the p-adaptive method in Figure 20 is then valued by the significant difference in the prominent frequency and peak displacement responses. These variations lead to a distinct nonlinear behavior devised in Figure 22. The nonlinear behavior was identified when some rebar fiber yields at the end of each element. Figure 22 illustrates the structural damage patterns for second-order elements and those refined using the p-adaptive method. Green segments indicate yielding at element ends, while red segments represent failed elements, such as the masonry in Building 5.

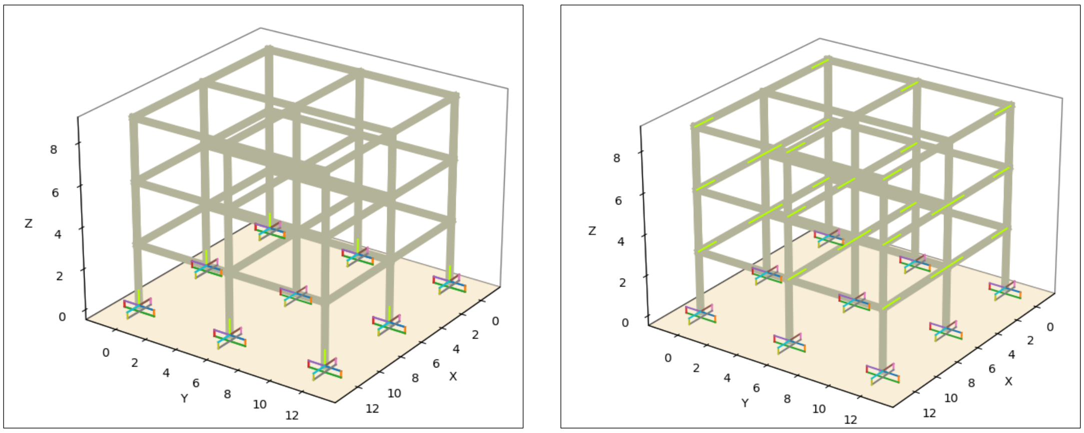

Building 1

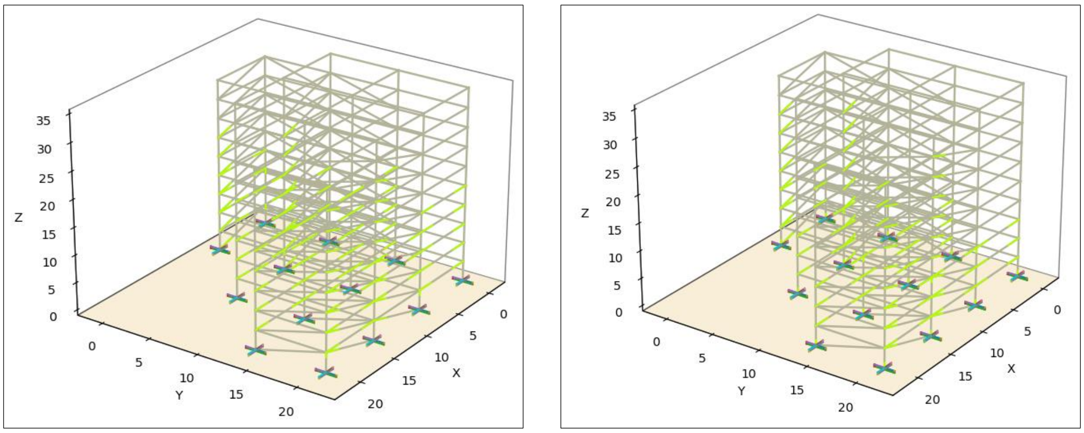

Building 2

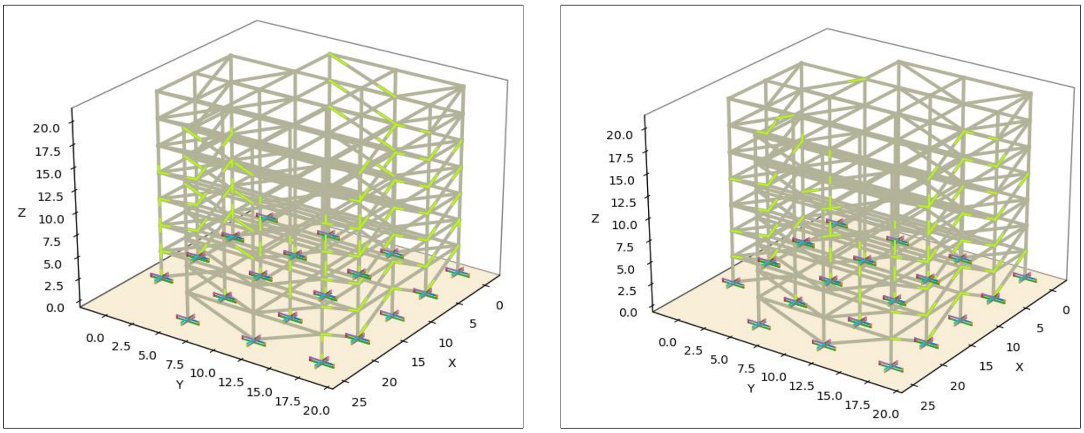

Building 3

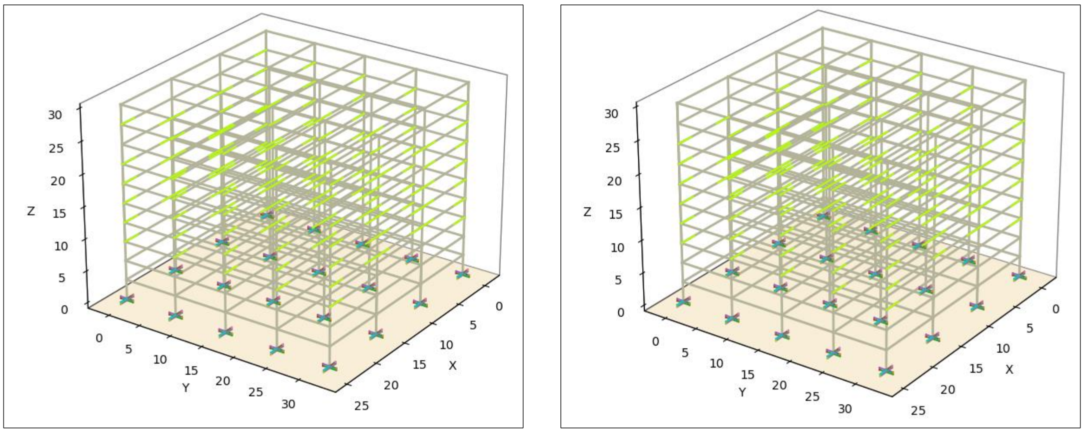

Building 4

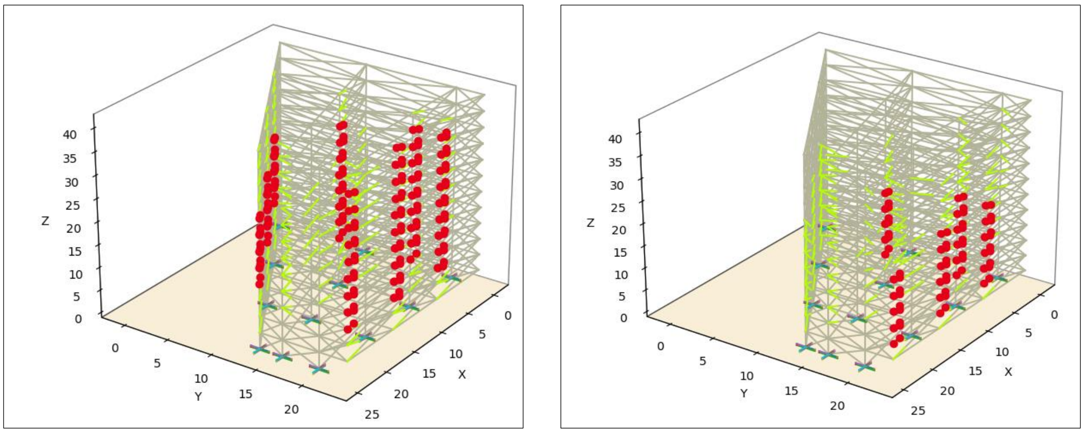

Building 5

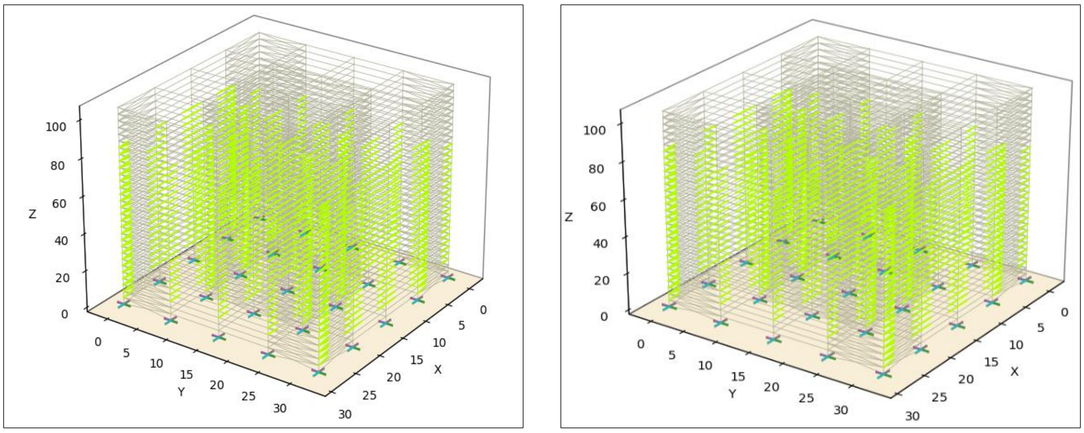

Building 6

Figure 22. Comparison of the nonlinear behavior of the buildings between analyses with (right column) and without (left column) the p-adaptive method

It can be seen in Figure 22 that there are many differences in the nonlinear behavior of the buildings using and not using the p-adaptive method. In an overview, there are errors of 135% of elements yielding for Building 1, 14% for Building 2, 31% for Building 3, 6% for Building 4, 55% for Building 5, and 7% for Building 6. The significant difference in Building 1 is due to the large dissimilitude shown in the frequency and amplitude diagrams. Another significant difference is found in Building 5, which occurs due to the weakness of the masonry. All these results demonstrate the need to refine the mesh for structural analysis using the p-adaptive method considering the round-off error since the nonlinear behavior is different.

After using the p-adaptive method, the structure's natural periods remained the same using the Ritz modes in the X-direction:

- Building 1: 1.05 for mode one, 0.32 for mode two, and 0.17 for mode three.
- Building 2: 2.42 for mode one, 2.07 for mode two, and 0.59 for mode three.
- Building 3: 0.81 for mode one, 0.27 for mode two, and 0.14 for mode three.
- Building 4: 1.19 for mode one, 1.10 for mode two, and 0.35 for mode three.
- Building 5: 1.70 for mode one, 1.47 for mode two, and 0.42 for mode three.
- Building 6: 4.89 for mode one, 4.73 for mode two, and 1.48 for mode three.

Even after obtaining the same natural periods, it can be noticed in the fast Fourier results that the displacement diagram frequencies tend to be higher. The reasons may be varied; for instance, the p-adaptive method might refine the mesh in specific regions, leading to a more accurate representation of local stiffness and mass properties. High-order shape functions could subtly alter the structure's dynamic behavior, resulting in a shift in the dominant frequencies. Moreover, when the material model used in the analysis is nonlinear, the p-adaptive method refines the mesh in regions where the material will experience significant nonlinear behavior. This nonlinearity may change the structure's stiffness properties, affecting the dynamic response and the fast Fourier results.

One of the objectives of using the p-adaptive method is not to affect the running time excessively. Thus, the times recorded for each analysis are listed in Table 3.

Table 3. Running time in minutes in the examples

Building	No p-adaptive, Grubbs	p-adaptive, Grubbs	OpenSees
1	12.445	12.785	2.110
2	64.980	58.865	25.818
3	120.331	111.355	No convergence
4	97.703	100.354	89.178
5	105.493	111.519	124.496
6	386.213	381.028	4776.08 (3.31 days)

The running time in the models depends on the iterations in the numerical method and the nonlinear evaluation, which explains the differences between the "No p-adaptive, Grubbs" and "p-adaptive, Grubbs" models. The made software starts evaluating the real rigidities in each section once any element is near yield, according to Monti & Petrone [54] limits, so the "No p-adaptive, Grubbs" method takes longer in some examples. The disparities oscillate between 1% and 10%, which can be considered a low difference. This variation is difficult to predict since, as the complexity of the structure increases, so does the rounding error, which limits the number of elements that can be refined (see flowchart of this study's procedure has been included at the end of Section 2). The entire dynamic behavior could also change. Even without considering the round-off error that depends on the machine because refinement is not intrinsic to the structure but relies on the loads.

Conversely, significant distinctions have been found between the developed software and OpenSees. One reason is that the developed software was made entirely in the high-level language Python 3 and OpenSees in the low-level language C++, in addition to many other differences. Thus, OpenSees proved to be a fast software for analyzing relatively small structures, as fast as 490% compared to the developed software. On the other hand, the developed software proved to be fast for calculating large buildings; the difference is 1137%.

6. Conclusion

This research identified a truncation error associated with shape function order, a frequently overlooked issue in structural analyses of buildings and other infrastructure. To address this, the study developed equations for calculating truncation errors. Furthermore, as existing methods for determining nonlinear plastic length in high-order elements were limited, a novel approach using sigmoid function sets was presented. This approach provides a more accurate representation of material behavior under complex loading conditions.

The p-adaptive procedure was adapted for nonlinear dynamic analyses, deviating from its traditional application to static analysis. To accurately capture dynamic behavior, inertial and damping internal forces were incorporated in addition to restitutive internal forces. These additional considerations are crucial for modeling the complex response of structures subjected to dynamic loads, such as earthquakes. Complex structures subjected to dynamic analysis often exhibit numerical instability. This study proposed a method to filter out irrelevant modal shapes using Ritz modes, which were then used to reconstruct the mass matrix. This approach effectively improves the stability and accuracy of the analysis by focusing on the dominant modes that contribute significantly to the structural response. The examples demonstrated that even in simple cases, reducing truncation error impacts structural responses significantly, emphasizing the importance of mesh refinement for accurate analysis. Moreover, the study found that the computational time for the p-adaptive method remained comparable to traditional methods, with a maximum difference of 10% in the analyzed examples. This efficiency is particularly important for large-scale and complex structural analyses where computational time is a critical factor.

7. Declarations

7.1. Author Contributions

Conceptualization, E.D.M.M. and N.K.; methodology, E.D.M.M. and N.K.; software, E.D.M.M.; validation, E.D.M.M. and N.K.; formal analysis, E.D.M.M. and N.K.; investigation, E.D.M.M. and N.K. resources, E.D.M.M. and N.K.; data curation, E.D.M.M.; writing—original draft preparation, E.D.M.M.; writing—review and editing, N.K.; visualization, E.D.M.M. and N.K.; supervision, N.K.; project administration, N.K.; funding acquisition, E.D.M.M. and N.K. All authors have read and agreed to the published version of the manuscript.

7.2. Data Availability Statement

The data presented in this study are available in the article.

7.3. Funding and Acknowledgement

This research has been supported through the SDGs Global Leader Program JFY2021 funding under JICA's Knowledge Co-Creation Program (Long-Term), ID: D2101987. This support is gratefully acknowledged.

7.4. Conflicts of Interest

The authors declare no conflict of interest.

8. References

[1] Fang, L. (2021). Error Estimation and Adaptive Refinement of Finite Element Thin Plate Spline. Ph.D. Thesis, Australian National University, Canberra, Australia.

[2] Dong, Y., Yuan, S., & Xing, Q. (2019). Adaptive finite element analysis with local mesh refinement based on a posteriori error estimate of element energy projection technique. Engineering Computations (Swansea, Wales), 36(6), 2010–2033. doi:10.1108/EC-11-2018-0523.

[3] Eisenträger, S., Atroshchenko, E., & Makvandi, R. (2020). On the condition number of high order finite element methods: Influence of p-refinement and mesh distortion. Computers and Mathematics with Applications, 80(11), 2289–2339. doi:10.1016/j.camwa.2020.05.012.

[4] Wilson, S. G., Eaton, M. D., & Kópházi, J. (2024). Energy-Dependent, Self-Adaptive Mesh h(p)-Refinement of a Constraint-Based Continuous Bubnov-Galerkin Isogeometric Analysis Spatial Discretization of the Multi-Group Neutron Diffusion Equation with Dual-Weighted Residual Error Measures. Journal of Computational and Theoretical Transport, 53(2), 89–152. doi:10.1080/23324309.2024.2313460.

[5] De Domenico, D., Ricciardi, G., & Takewaki, I. (2019). Design strategies of viscous dampers for seismic protection of building structures: A review. Soil Dynamics and Earthquake Engineering, 118, 144–165. doi:10.1016/j.soildyn.2018.12.024.

[6] Sun, B., Zhang, Y., Dai, D., Wang, L., & Ou, J. (2023). Seismic fragility analysis of a large-scale frame structure with local nonlinearities using an efficient reduced-order Newton-Raphson method. Soil Dynamics and Earthquake Engineering, 164. doi:10.1016/j.soildyn.2022.107559.

[7] Chatterjee, T., & Chowdhury, R. (2018). H–P Adaptive Model Based Approximation of Moment Free Sensitivity Indices. Computer Methods in Applied Mechanics and Engineering, 332, 572–599. doi:10.1016/j.cma.2018.01.011.

[8] Bai, R., Gao, W. L., Liu, S. W., & Chan, S. L. (2020). Innovative high-order beam-column element for geometrically nonlinear analysis with one-element-per-member modelling method. Structures, 24, 542–552. doi:10.1016/j.istruc.2020.01.036.

[9] Sharifnia, M. (2022). A higher-order nonlinear beam element for planar structures by using a new finite element approach. Acta Mechanica, 233(2), 495–511. doi:10.1007/s00707-021-03076-4.

[10] Ho, P. L. H., Lee, C., Le, C. V., Nguyen, P. H., & Yee, J. J. (2024). A computational homogenization for yield design of asymmetric microstructures using adaptive BES-FEM. Computers and Structures, 294. doi:10.1016/j.compstruc.2023.107271.

[11] Moslemi, H., & Tavakkoli, A. (2018). A Statistical Approach for Error Estimation in Adaptive Finite Element Method. International Journal for Computational Methods in Engineering Science and Mechanics, 19(6), 440–450. doi:10.1080/15502287.2018.1558424.

[12] Gui, Q., Li, W., & Chai, Y. (2024). Improved modal analyses using the novel quadrilateral overlapping elements. Computers and Mathematics with Applications, 154, 138–152. doi:10.1016/j.camwa.2023.11.027.

[13] Chopra, A. K. (2020). Dynamics Of Structures, Theory and Applications to Earthquake Engineering (5^{th} Ed.). Pearson, Harlow, United Kingdom.

[14] Ren, Z., He, Z., & Qi, Z. (2020). A temporal hybrid dynamic integration algorithm strategy for inelastic time history analysis of high-rise reinforced concrete structures under strong earthquakes. Structural Design of Tall and Special Buildings, 29(2), e1690. doi:10.1002/tal.1690.

[15] He, Z., Ren, Z., Qi, Z., & Fu, S. (2021). A temporal–spatial hybrid dynamic algorithm strategy for inelastic earthquake response analysis of super high-rise building structures. Structural Design of Tall and Special Buildings, 30(14), e1885. doi:10.1002/tal.1885.

[16] Hassan, M. M., Van Nguyen, D., Wook Choo, Y., & Kim, D. (2024). A simplified approach of numerical seismic model updating for deep braced excavation using centrifuge test. Results in Engineering, 21. doi:10.1016/j.rineng.2024.101849.

[17] Liu, T., Huang, F., Wen, W., He, X., Duan, S., & Fang, D. (2021). Further insights of a composite implicit time integration scheme and its performance on linear seismic response analysis. Engineering Structures, 241. doi:10.1016/j.engstruct.2021.112490.

[18] Bovo, M., Savoia, M., & Praticò, L. (2021). Seismic Performance Assessment of a Multistorey Building Designed with an Alternative Capacity Design Approach. Advances in Civil Engineering, 5178065. doi:10.1155/2021/5178065.

[19] Chalarca, B., Filiatrault, A., & Perrone, D. (2024). Expected seismic response and annual seismic loss of viscously damped braced steel frames. Engineering Structures, 303. doi:10.1016/j.engstruct.2024.117569.

[20] Ballinas, E., Guerrero, H., Terán-Gilmore, A., & Alberto Escobar, J. (2021). Seismic response comparison of an existing hospital structure rehabilitated with BRBs or conventional braces. Engineering Structures, 243. doi:10.1016/j.engstruct.2021.112666.

[21] Belytschko, T., Liu, W. K., Moran, B., & Elkhodary, K. (2014). Nonlinear finite elements for continua and structures. John Wiley & Sons, Hoboken, United States.

[22] Eldin, M. N., Dereje, A. J., & Kim, J. (2020). Seismic retrofit of RC buildings using self-centering PC frames with friction-dampers. Engineering Structures, 208. doi:10.1016/j.engstruct.2019.109925.

[23] De Angeli, S., Malamud, B. D., Rossi, L., Taylor, F. E., Trasforini, E., & Rudari, R. (2022). A multi-hazard framework for spatial-temporal impact analysis. International Journal of Disaster Risk Reduction, 73. doi:10.1016/j.ijdrr.2022.102829.

[24] Gentile, R., & Galasso, C. (2021). Simplicity versus accuracy trade-off in estimating seismic fragility of existing reinforced concrete buildings. Soil Dynamics and Earthquake Engineering, 144. doi:10.1016/j.soildyn.2021.106678.

[25] Abuteir, B. W., Harkati, E., Boutagouga, D., Mamouri, S., & Djeghaba, K. (2022). Thermo-mechanical nonlinear transient dynamic and Dynamic-Buckling analysis of functionally graded material shell structures using an implicit conservative/decaying time integration scheme. Mechanics of Advanced Materials and Structures, 29(27), 5773–5792. doi:10.1080/15376494.2021.1964115.

[26] Song, C., Eisenträger, S., & Zhang, X. (2022). High-order implicit time integration scheme based on Padé expansions. Computer Methods in Applied Mechanics and Engineering, 390(2022), 1–43. doi:10.1016/j.cma.2021.114436.

[27] Ji, Y., & Xing, Y. (2022). A two-step time integration method with desirable stability for nonlinear structural dynamics. European Journal of Mechanics, A/Solids, 94(2022), 1–19. doi:10.1016/j.euromechsol.2022.104582.

[28] Nejati, F., Ghani, A. A. A., Yap, N. K., & Jafaar, A. Bin. (2021). Handling State Space Explosion in Component-Based Software Verification: A Review. IEEE Access, 9, 77526–77544. doi:10.1109/ACCESS.2021.3081742.

[29] Lee, C., Bathe, K. J., & Noh, G. (2024). Stability of the Bathe implicit time integration methods in the presence of physical damping. Computers and Structures, 295. doi:10.1016/j.compstruc.2024.107294.

[30] Lavrenčič, M., & Brank, B. (2020). Comparison of numerically dissipative schemes for structural dynamics: Generalized-alpha versus energy-decaying methods. Thin-Walled Structures, 157(2020), 1–22. doi:10.1016/j.tws.2020.107075.

[31] Jančič, M., & Kosec, G. (2024). Strong form mesh-free p-adaptive solution of linear elasticity problem. Engineering with Computers, 40(2), 1027–1047. doi:10.1007/s00366-023-01843-6.

[32] Mora, E. D., & Khaji, N. (2023). Complexity Adaptation Strategy for Order-Adaptive Elements. Proceedings of the Seventeenth International Conference on Civil, Structural and Environmental Engineering Computing, 6, 1–10. doi:10.4203/ccc.6.13.5.

[33] IEEE. (2019)."IEEE Standard for Floating-Point Arithmetic," in IEEE Std. 754-2019 (Revision of IEEE 754-2008), 1-84, 22 July 2019. doi:10.1109/IEEESTD.2019.8766229.

[34] Ribeiro Almeida, L. P., Souza Santana, H. M., & da Rocha, F. C. (2020). Analysis of high-order approximations by spectral interpolation applied to one-and two-dimensional finite element method. Journal of Applied and Computational Mechanics, 6(1), 145–159. doi:10.22055/jacm.2019.28771.1511.

[35] Chen, G., Qian, L., & Yin, Q. (2014). Dynamic analysis of a timoshenko beam subjected to an accelerating mass using spectral element method. Shock and Vibration, 2014, 1–12. doi:10.1155/2014/768209.

[36] Felippa, C. A., & Oñate, E. (2021). Accurate Timoshenko Beam Elements for Linear Elastostatics and LPB Stability. Archives of Computational Methods in Engineering, 28(3), 2021–2080. doi:10.1007/s11831-020-09515-0.

[37] Katili, I. (2017). Unified and integrated approach in a new Timoshenko beam element. European Journal of Computational Mechanics, 26(3), 282–308. doi:10.1080/17797179.2017.1328643.

[38] Moallemi-Oreh, A., & Karkon, M. (2013). Finite element formulation for stability and free vibration analysis of timoshenko beam. Advances in Acoustics and Vibration, 2013, 1–7. doi:10.1155/2013/841215.

[39] Öchsner, A. (2020). Euler–Bernoulli Beams and Frames. Computational Statics and Dynamics, Springer, Singapore. doi:10.1007/978-981-15-1278-0_3.

[40] Liu, J., Möller, M., & Schuttelaars, H. M. (2021). Balancing truncation and round-off errors in FEM: One-dimensional analysis. Journal of Computational and Applied Mathematics, 386. doi:10.1016/j.cam.2020.113219.

[41] Cheney, W., & Kingaid, D. (2012). Numerical Mathematics and Computing (7th Ed.). Cengage Learning, Boston, United States.

[42] Paige, C. C., & Saunders, M. A. (1982). LSQR: An Algorithm for Sparse Linear Equations and Sparse Least Squares. ACM Transactions on Mathematical Software (TOMS), 8(1), 43–71. doi:10.1145/355984.355989.

[43] Bruschi, E., Calvi, P. M., & Quaglini, V. (2021). Concentrated plasticity modelling of RC frames in time-history analyses. Engineering Structures, 243. doi:10.1016/j.engstruct.2021.112716.

[44] Mazza, F. (2014). A distributed plasticity model to simulate the biaxial behaviour in the nonlinear analysis of spatial framed structures. Computers and Structures, 135, 141–154. doi:10.1016/j.compstruc.2014.01.018.

[45] Park, K., Kim, H., & Kim, D. J. (2019). Generalized Finite Element Formulation of Fiber Beam Elements for Distributed Plasticity in Multiple Regions. Computer-Aided Civil and Infrastructure Engineering, 34(2), 146–163. doi:10.1111/mice.12389.

[46] Ahmed, M., Liang, Q. Q., Patel, V. I., & Hamoda, A. (2024). Inelastic analysis of octagonal concrete-filled steel tubular short columns under eccentric loading. Structural Concrete, 25(2), 1418–1433. doi:10.1002/suco.202300360.

[47] Zhang, H., Han, Q., Wang, Y., & Lu, Y. (2016). Explicit modeling of damping of a single-layer latticed dome with an isolation system subjected to earthquake ground motions. Engineering Structures, 106, 154–165. doi:10.1016/j.engstruct.2015.10.027.

[48] Tian, K., Wang, Y., Cao, D., & Yu, K. (2024). Approximate global mode method for flutter analysis of folding wings. International Journal of Mechanical Sciences, 265. doi:10.1016/j.ijmecsci.2023.108902.

[49] Chaikittiratana, A., & Wattanasakulpong, N. (2022). Gram-Schmidt-Ritz method for dynamic response of FG-GPLRC beams under multiple moving loads. Mechanics Based Design of Structures and Machines, 50(7), 2427–2448. doi:10.1080/15397734.2020.1778488.

[50] Du, X., Nie, Y., Xia, H., Zhang, N., & Guo, W. (2022). A single-step recursive representation of foundation flexibility functions to soil-structure interaction using first-order IIR filters. Soil Dynamics and Earthquake Engineering, 153. doi:10.1016/j.soildyn.2021.107123.

[51] Chang, T. L., & Lee, C. L. (2022). Numerical simulation of generalised Maxwell-type viscous dampers with an efficient iterative algorithm. Mechanical Systems and Signal Processing, 170. doi:10.1016/j.ymssp.2021.108795.

[52] Haghani, M., Navayi Neya, B., Ahmadi, M. T., & Vaseghi Amiri, J. (2020). Combining XFEM and time integration by α-method for seismic analysis of dam-foundation-reservoir. Theoretical and Applied Fracture Mechanics, 109. doi:10.1016/j.tafmec.2020.102752.

[53] Yang, J., Xia, Y., Lei, X., & Sun, L. (2022). Hysteretic parameters identification of RC frame structure with Takeda model based on modified CKF method. Bulletin of Earthquake Engineering, 20(9), 4673–4696. doi:10.1007/s10518-022-01368-1.

[54] Monti, G., & Petrone, F. (2015). Yield and ultimate moment and curvature closed-form equations for reinforced concrete sections. ACI Structural Journal, 112(4), 463–474. doi:10.14359/51687747.

[55] SeismoStruct. (2010). A computer program for static and dynamic nonlinear analysis of framed structures. Seismosoft Earthquake Engineering Software Solutions - Seismosoft, Pavia, Italy.

[56] Zhu, M., McKenna, F., & Scott, M. H. (2018). OpenSeesPy: Python library for the OpenSees finite element framework. SoftwareX, 7(2018), 6–11. doi:10.1016/j.softx.2017.10.009.

[57] Pankrath, H., Mora, D., Jiménez, E., Knut, A., & Sandig, F. (2020). Development of shaking table tests for seismic slope stability problems. SCG-XIII International Symposium on Landslides, 15-19 June, 2020, Cartagena, Colombia.

[58] Joseph, R., Mwafy, A., & Alam, M. S. (2023). Shake-table testing and numerical simulation to select the FRCM retrofit solution for flexure/shear deficient RC frames. Journal of Building Engineering, 69. doi:10.1016/j.jobe.2023.106248.

[59] Mwafy, A., & Almorad, B. (2019). Verification of performance criteria using shake table testing for the vulnerability assessment of reinforced concrete buildings. Structural Design of Tall and Special Buildings, 28(7), e1601. doi:10.1002/tal.1601.

[60] Krawinkler, H. (1988). Scale effects in static and dynamic model testing of structures. Proceedings of the Ninth World Conference on Earthquake Engineering, 2-9 August, 1988, Tokyo, Japan.

[61] Zhang, N., Gu, Q., Huang, S., Chang, R., & Yang, T. Y. (2023). A smart component model replacement approach for refined simulation of large nonlinear RC structures. Computers and Structures, 289. doi:10.1016/j.compstruc.2023.107184.

[62] Abtahi, S., & Li, Y. (2023). Efficient modeling of steel bar slippage effect in reinforced concrete structures using a newly implemented nonlinear element. Computers and Structures, 279. doi:10.1016/j.compstruc.2022.106958.

[63] Valipour, H. R., & Foster, S. J. (2009). Nonlocal Damage Formulation for a Flexibility-Based Frame Element. Journal of Structural Engineering, 135(10), 1213–1221. doi:10.1061/(asce)st.1943-541x.0000054.